

# The Sunburst Arc with JWST: II. Observations of an Eta Carinae Analog at $z = 2.37$

S. Choe<sup>1\*</sup>, T. Emil Rivera-Thorsen<sup>1</sup>, H. Dahle<sup>2</sup>, K. Sharon<sup>3</sup>, M. Riley Owens<sup>4</sup>, J. R. Rigby<sup>5</sup>, M. B. Bayliss<sup>4</sup>, M. J. Hayes<sup>1</sup>, T. Hutchison<sup>5</sup>, B. Welch<sup>5,6,7</sup>, J. Chisholm<sup>8</sup>, M. D. Gladders<sup>9,10</sup>, and G. Khullar<sup>11</sup>  
K. Kim<sup>12</sup>

<sup>1</sup> The Oskar Klein Centre, Department of Astronomy, Stockholm University, AlbaNova 10691, Stockholm, Sweden

<sup>2</sup> Institute of Theoretical Astrophysics, University of Oslo, P.O. Box 1029, Blindern, NO-0315 Oslo, Norway

<sup>3</sup> Department of Astronomy, University of Michigan, 1085 S. University Ave, Ann Arbor, MI 48109, USA

<sup>4</sup> Department of Physics, University of Cincinnati, Cincinnati, OH 45221, USA

<sup>5</sup> Astrophysics Science Division, Code 660, NASA Goddard Space Flight Center, 8800 Greenbelt Rd., Greenbelt, MD 20771, USA

<sup>6</sup> Department of Astronomy, University of Maryland, College Park, MD 20742, USA

<sup>7</sup> Center for Research and Exploration in Space Science and Technology, NASA/GSFC, Greenbelt, MD 20771

<sup>8</sup> Department of Astronomy, University of Texas at Austin, 2515 Speedway, Austin, Texas 78712, USA

<sup>9</sup> Department of Astronomy and Astrophysics, University of Chicago, 5640 South Ellis Avenue, Chicago, IL 60637, USA

<sup>10</sup> Kavli Institute for Cosmological Physics, University of Chicago, Chicago, IL 60637, USA

<sup>11</sup> Department of Physics and Astronomy and PITT PACC, University of Pittsburgh, Pittsburgh, PA 15260, USA

<sup>12</sup> IPAC, California Institute of Technology, 1200 E. California Blvd., Pasadena CA, 91125, USA

Received April 2024

## ABSTRACT

**Context.** “Godzilla” is a peculiar object within the gravitationally lensed Sunburst Arc at  $z = 2.37$ . Despite being very bright, it appears in only one of the twelve lensed images of the source galaxy, and shows exotic spectroscopic properties not found elsewhere in the galaxy.

**Aims.** We use JWST’s unique combination of spatial resolution and spectroscopic sensitivity to provide a unified, coherent explanation of the physical nature of Godzilla.

**Methods.** We measure fluxes and kinematic properties of rest-optical emission lines in Godzilla and surrounding regions. Using standard line ratio-based diagnostic methods in combination with NIRC*am* imaging and ground based rest-UV spectra, we characterize Godzilla and its surroundings.

**Results.** We find that Godzilla is most likely an extremely magnified, non-erupting LBV star with dense gas condensations in close proximity. Among around 60 detected lines, we find a cascade of strong O I lines pumped by intense Ly $\beta$  emission, as well as Ly $\alpha$ -pumped rest-optical Fe II lines, reminiscent of the Weigelt blobs in the local LBV star Eta Carinae. Godzilla is surrounded by dusty, inhomogeneous gas common to massive, evolved stars. Spectra and images of Godzilla and adjacent objects and the detection of a low-surface brightness foreground galaxy in the NIRC*am* data support the interpretation that Godzilla is a stellar-scale object extremely magnified by alignment with lensing caustics. To explain the dusty surroundings, strong [Ne III] and line kinematics simultaneously, we argue that Godzilla is a post-eruption LBV accompanied by a hotter companion and/or gas condensations exposed to more intense radiation compared to the Weigelt blobs. We expect periodic spectroscopic variations if Godzilla is a binary system. If Godzilla is confirmed to be an LBV star, it expands the distance to the furthest known LBV from a dozen Mpc to several Gpc.

**Key words.** galaxies: ISM – galaxies: individual: Sunburst Arc – (stars:) circumstellar matter – stars: massive

## 1. Introduction

Gravitational lensing magnifies distant objects. For a sufficiently small source (e.g. a single star), the magnification from a smooth galaxy cluster-scale lens can reach extreme factors ( $10^3 - 10^6$ , Miralda-Escude 1991). In realistic cluster-scale lenses, theoretical work has found that “microlenses”, small-scale masses (e.g. stars) within the lensing cluster, perturb the lensing potential near the primary caustics, creating a web of micro-caustics. These microcaustics cause the total magnification of the background lensed star to fluctuate, and also tend to limit the maximum magnification achievable (Venumadhav et al. 2017; Diego et al. 2018; Diego 2019).

The first lensed stars at cosmological distances ( $z \sim 1 - 1.5$ ) were discovered as transients in Hubble Space Telescope (HST) imaging, their magnifications fluctuating as a result of microlensing (Kelly et al. 2018; Rodney et al. 2018; Kaurov et al. 2019; Chen et al. 2019). Since these initial discoveries, many more lensed stars have been found using this transient method (e.g., Kelly et al. 2022; Fudamoto et al. 2024). Additionally, several lensed stars have been identified from their proximity to the lensing critical curve (e.g., Meena et al. 2023; Diego et al. 2023a,b), including the most distant lensed star yet discovered at  $z \sim 6$  (Welch et al. 2022a,b).

Thus far, spectroscopic studies of lensed stars have proven difficult, owing to their transient nature or faintness. Furtak et al. (2024) present the James Webb Space Telescope (JWST) NIR-Spec prism spectroscopy of a lensed star at  $z = 4.76$ , however

\* Corresponding author; e-mail: suhyeon.choe@astro.su.se

they only detect stellar continuum, making it difficult to draw precise conclusions on the nature of the star.

In this paper, we study a lensed star candidate in the Sunburst Arc galaxy at  $z = 2.37$ . The Sunburst Arc is the brightest known strongly lensed galaxy at optical wavelengths, with an integrated magnitude  $m_{AB} \lesssim 18$  (Dahle et al. 2016) and dozens of highly magnified and multiply imaged star-forming regions (Sharon et al. 2022). The Sunburst Arc earns its name from the strong “direct escape” Lyman- $\alpha$  ( $Ly\alpha$ ) emission (Rivera-Thorsen et al. 2017) and high fraction of Lyman Continuum (LyC) radiation escaping along the line of sight (LOS) from a single star-forming region (Rivera-Thorsen et al. 2019).

As a result of strong gravitational lensing, unresolved features in the Sunburst Arc (clumps or knots) are replicated multiple times along the arc. For example, the LyC-emitting clump (Sunburst LCE) shows an unusually extensive collection of 12 copied images. One unique clump as bright as Sunburst LCE, however, does not appear to have a counterpart anywhere else (Figure 1). Vanzella et al. (2020) found that this singly-imaged source in the northwest arc also exhibits highly unusual rest-ultraviolet (UV) features, such as Fe II emission lines excited by  $Ly\alpha$  pumping (Bowen fluorescence, Bowen 1934), and has very high electron density  $n_e \gtrsim 10^6 \text{ cm}^{-3}$  probed by carbon and silicon emission doublets. Vanzella et al. (2020) first denoted this object as “Tr”, meaning transient. Diego et al. (2022) followed this notation while dubbing the object “Godzilla”, and Sharon et al. (2022) referred to it as “a discrepant clump”. Recently, Pascale & Dai (2024) also adopted the name Godzilla, so we use this term in this paper for the sake of a homogeneous terminology. For arcs and the IDs of the lensed images of clumps, we adopt the terminology of Sharon et al. (2022).

Godzilla is believed to be an object residing in the Sunburst Arc galaxy, as its spectroscopic redshift is the same as the Sunburst Arc ( $z \approx 2.37$ ). The absence of any counterimages of Godzilla can be explained by an additional microlensing effect (Weisenbach et al. 2024) caused by a small object in front of Godzilla, extremely magnifying it only at that position (Diego et al. 2022; Sharon et al. 2022). An earlier explanation of Godzilla as a transient such as a supernova (SN) (Vanzella et al. 2020) has since been ruled out (Sharon et al. 2022). Sharon et al. demonstrated that Godzilla did not clearly fade from February 2018 to December 2020 in HST imaging (Figure 9 therein). Godzilla maintained its luminosity for around a year in the rest-frame, correcting for cosmological time dilation. This significantly weakens the scenario of a SN interacting with its circumstellar medium (CSM), as suggested by Vanzella et al. (2020). The SN scenario also contradicts the maximum time delay predicted from the lens model by Sharon et al. (2022). Relative time delays between the north arc and the northwest and west arcs are less than a year (Sharon et al. 2022, Figure 8), so counterimages of Godzilla should have been observed in other arcs if Godzilla were a SN. Pascale & Dai (2024) argues that Godzilla is a young, massive star cluster from spectral energy distribution (SED) fitting, but the absence of Godzilla’s counterimages is not clearly explained in that work.

Previous studies on Godzilla gave special attention to  $\eta$  Carinae ( $\eta$  Car), a Luminous Blue Variable (LBV) star in the Milky Way, as a possible analog. LBV is an umbrella term that includes previously defined Hubble-Sandage Variables, S Dor Variables, P Cyg and  $\eta$  Car type stars as sub-types, and specifically excludes Wolf-Rayet stars and blue supergiants (Conti 1984; Weis & Bomans 2020). LBVs are massive evolved stars (Weis & Bomans 2020, see their Figure 3) often surrounded by circumstellar nebulae as a consequence of their high mass loss rate (Weis &

Bomans 2020). These hot, unstable stars occupy an inclined instability strip of  $-11 \leq M_{bol} \leq -9$  and  $14,000 \leq T_{eff} \leq 35,000\text{K}$  in the Hertzsprung-Russell (HR) diagram when they are quiescent, i.e. not erupting (S Dor cycle, Wolf 1989). In some cases, they undergo “giant eruptions” where the brightness increases by several magnitudes, as spectacularly observed for  $\eta$  Car in the year 1843 (“The Great Eruption”, Humphreys et al. 1999) or in P Cygni in the 17th century (de Groot 1988). In that event,  $\eta$  Car brightened to  $m_V \approx -1$  (currently  $m_V \approx 4.0^1$ ) and ejected at least  $10 M_{\odot}$ , forming the Homunculus nebula (Davidson & Humphreys 2012, Ch. 7). Diego et al. (2022) demonstrated that the observed brightness of Godzilla can be achieved assuming a magnification factor of  $\mu \approx 7000$  and an intrinsic brightness similar to that of  $\eta$  Car during the Great Eruption.

Vanzella et al. (2020) also pointed out that the  $Ly\alpha$ -pumped Fe II  $\lambda 1914$  detected in Godzilla has been observed in the Weigelt blobs in  $\eta$  Car (Johansson & Letokhov 2005). Weigelt & Ebersberger (1986) first discovered these three star-like gas condensations with diameters of  $< 0.03''$  ( $\sim 70$  AU for a distance of 2300 pc) located within  $0.1'' - 0.2''$  ( $\sim 230 - 460$  AU) from  $\eta$  Car using speckle interferometry. In 1995, HST resolved them in spectroscopy (Davidson & Humphreys 2012, Ch. 1.4) and revealed that they are slowly moving with a line-of-sight velocity of  $\sim 40 \text{ km s}^{-1}$ , have densities of  $10^7 - 10^8 \text{ cm}^{-3}$ , and temperatures of  $6,000 - 7,000 \text{ K}$  (Davidson & Humphreys 2012, Ch. 5). HST spectroscopy also revealed the 5.54-year spectroscopic cycle of  $\eta$  Car (Damineli 1996), where high excitation lines weaken when the hotter secondary star ( $40 - 50 M_{\odot}$ ,  $\sim 4 \times 10^5 L_{\odot}$ ,  $T_{eff} \approx 39,000\text{K}$ ; Mehner et al. 2010) hides behind the more massive, cooler primary star ( $\gtrsim 90 M_{\odot}$ ,  $\sim 10^{6.7} L_{\odot}$ ,  $T_{eff} \sim 20,000 \text{ K}$ ; Davidson & Humphreys 2012, 1.3.1). Along with high excitation lines,  $Ly\alpha$ -pumped and  $Ly\beta$ -pumped lines such as Fe II  $\lambda 8453$ , Fe II  $\lambda 8490$  and O I  $\lambda 8449$  strengthen when the Weigelt blobs are exposed to the hotter secondary star (Davidson & Humphreys 2012, Figure 5.4).

The origin of the Weigelt blobs is the subject of ongoing research. It has been previously believed that the Weigelt blobs were formed during a brightening in 1941 (Davidson & Humphreys 2012; Abraham et al. 2014). Abraham et al. (2020) use Atacama Large Millimeter Array (ALMA) observations to better constrain the proper motion (and hence the formation time) of the Weigelt blobs. They find that the three blobs are formed at different times (see their Fig.16), but in each case the blob formation coincides with epochs of minimum intensity in high-ionisation lines in the spectrum of  $\eta$  Car. These epochs are also thought to coincide with the periastron of the hotter companion. There do not seem to be particularly noticeable enhancements of the overall brightness of eta Car during these epochs (see e.g. the V-band/visual light curve in Fig. 3 of Fernández-Lajús et al. 2009).

Detecting extragalactic LBVs in spatially unresolved observations is highly challenging (Guseva et al. 2023). First, it is hard to capture the LBV phase of a star due to the short lifespan of this phase (Herrero et al. 2010,  $10^4 - 10^5$  years assuming single star evolution). Also, LBVs are not discernible from other bright hot stars during their quiescent phase, which can last for decades or centuries (Wofford et al. 2020). When they are not erupting, the S Dor variability is the only characteristic that distinguishes LBVs from other massive, evolved stars (Weis & Bomans 2020). For these reasons, only a handful of LBVs have been observed, and the farthest confirmed LBV is in DDO 68 which is 12.75

<sup>1</sup> Martin, J., 2024, Observations from the AAVSO International Database, <https://www.aavso.org>

Mpc away (Makarov et al. 2017). If Godzilla is really an LBV, then this discovery extends the farthest known individual LBV star from one at a dozen Mpc to several Gpc ( $z = 2.37$ ). However, many important traits of LBVs, such as broad hydrogen and often helium lines associated with P Cygni profiles (Guseva et al. 2023), emission line nebulae and dust nebulae often surrounding LBVs, are not possible to examine through ground-based telescopes at this redshift. Moreover, it was not possible to separate a pure spectrum of Godzilla uncontaminated by other features in previous ground-based slit spectroscopy. Thus, previous suggested explanations of Godzilla’s observed properties are based on the detection of a few exceptional emission lines or luminosity constraints from lens models. In this paper, we present JWST/NIRCam imaging and NIRSpect IFU observations of Godzilla for the first time. We have extracted the spatially resolved rest-optical to rest-near infrared (NIR) spectrum of Godzilla. Using imaging and spectroscopic data of unprecedented quality, we try to unveil the true nature of Godzilla.

The rest of this paper is structured as follows: in Section 2 we describe the observations and data reduction. In Section 3 we explain how we extracted spectra from Godzilla and four regions surrounding it. We also describe how we measured the kinematics and fluxes of emission lines, and corrected measured flux for dust reddening. In Section 4, we describe main results, including the detection of almost 60 emission lines, kinematics and gas properties of Godzilla, and detection of Ly $\beta$ -pumped O I  $\lambda$ 8449 and Ly $\alpha$ -pumped iron lines (Section 4.4). In Section 5, we discuss various aspects of Godzilla. We first take a look at the NIRCam image and revisit SN and microlensing scenarios (Section 5.1). Then we discuss spatial variations in the kinematics, dust, and gas properties by analyzing the surrounding regions (Section 5.2). We take a detailed look at the O I  $\lambda$ 8449 fluorescent line constraining the physical conditions of Godzilla (Section 5.3). Using spectroscopic constraints on the source energy, we examine other possibilities such as Very Massive Stars, Wolf-Rayet stars, and an intermediate-mass black hole (Section 5.4). Combining all this information, we suggest that Godzilla is most likely a post-eruption LBV possibly with a hot companion analogous to  $\eta$  Car (Section 6).

This paper assumes a flat  $\Lambda$ CDM cosmology with parameters  $\Omega_\Lambda = 0.7$ ,  $\Omega_m = 0.3$ , and  $H_0 = 70 \text{ km s}^{-1} \text{ Mpc}^{-1}$ . With this cosmology, the redshift of the source,  $z = 2.37$ , corresponds to 2.72 Gyr after the Big Bang.

## 2. Observations

JWST observed the Sunburst Arc with NIRCam imaging and NIRSpect integral field spectroscopy (IFS) in the interval April 4, 2023 to April 10, 2023 (JWST Cycle 1, GO-2555, PI: Rivera-Thorsen). Imaging was done in each of the NIRCam filters F115W, F150W, F200W, F277W, F356W, and F444W. Two NIRSpect grating and filter combinations, G140H/F100LP and G235H/F170LP, were used to cover a rest-frame wavelength range of  $0.29\mu\text{m} \leq \lambda_0 \leq 0.56\mu\text{m}$  and  $0.49\mu\text{m} \leq \lambda_0 \leq 0.94\mu\text{m}$ , respectively. Of the three on-target NIRSpect pointings, Godzilla is found in the pointing labeled 2 (the magenta square in Figure 1, indicated with an orange arrow). We refer to a companion paper by Rivera-Thorsen et al. (2024, in prep) for a full description of observations and data reduction.

This work also used observed-frame optical (rest-UV), ground-based spectra collected with the Magellan Echellette (MagE) spectrograph on the Magellan-I Baade Telescope of the Las Campanas Observatory in Chile. This spectrum is the slit M3 pointing displayed in Figure 1 of Mainali et al. (2022) that covers

Godzilla and two smaller, adjacent knots (the “P knots”, following the nomenclature of Diego et al. (2022)) seen in Figure 2. To summarize, we positioned slit M3 on the arc by comparing the MagE slit viewing camera and HST images, and reduced the data as described in Rigby et al. (2018). For more in-depth descriptions of the MagE observations and the reduction process, we refer to Owens et al. (2024, under review) for this pointing specifically, and Rigby et al. (in prep.) will present a complete observation log for each pointing of the parent MagE observation program.

## 3. Methods

### 3.1. Extraction of one dimensional spectra

We extracted spectra from the brightest center of Godzilla (Center), four regions surrounding it (NE, SE, NW, SW) to investigate spatial variations of gas properties (Figure 3), and the two P knots (named P1 and P2 for the left and right knot, respectively) for visual inspection. The spectra were extracted as a continuum-weighted spaxel average. The extracted spectrum of Center appears in the top panel of Figure 4, with prominent lines labeled. The Mikulski Archive for Space Telescopes (MAST) instrument pipeline appears to underestimate errors, considering that the pipeline errors are smaller than the standard deviation of line-masked continuum regions in the spectrum itself. To correct this, we added the standard deviation of an empty region of sky in quadrature with the pipeline’s error estimate. See Rivera-Thorsen et al. (2024, in prep.) for a more in-depth explanation. At the bottom panel of Figure 4, we show corrected uncertainties in the flux density for the G140H/F100LP and G235H/F170LP gratings in blue and red colors, respectively.

Before measuring fluxes, we subtracted the continua from the spectra. We first calculated the running-median and standard deviation ( $\sigma$ ) of the spectrum with a rest-frame 100 Å-wide moving window. After removing data outside  $3\sigma$ , we re-calculated the running median at the moving window, and subtracted that from the original spectrum.

### 3.2. Flux measurement

At Center, NW region, and SW region, we measured the flux of each line using two-component (narrow and broad) Gaussian fitting. Instrumental resolving power was accounted for by using the official NIRSpect calibration files<sup>2</sup>, and treating the linearly interpolated line spread function (LSF) as a Gaussian and adding that and the intrinsic linewidth in quadrature in the model. We first measured redshift and line width by fitting the strong oxygen doublet [O III]  $\lambda$ 4960 and [O III]  $\lambda$ 5008 simultaneously using a two-component Gaussian profile (Figure 3). Then we measured the flux of other lines in the same way (two-component Gaussian fitting), forcing each line to have the same redshift and velocity line width as measured for the [O III]  $\lambda$ 4960,5008 doublet at each grating. The error of the narrow, broad and total fluxes were separately estimated using a Monte Carlo sampling method. The flux measured from the unperturbed spectrum was taken as the nominal value. For each wave bin, we then drew 999 random samples from a normal distribution with  $(\mu, \sigma)$  being the observed flux density and the uncertainty in that bin, respectively, creating 999 perturbed spectra. We repeated fitting for the perturbed samples, and reported the standard deviation of the 1,000

<sup>2</sup> <https://jwst-docs.stsci.edu/jwst-near-infrared-spectrograph/nirspect-instrumentation/nirspect-dispersers-and-filters>

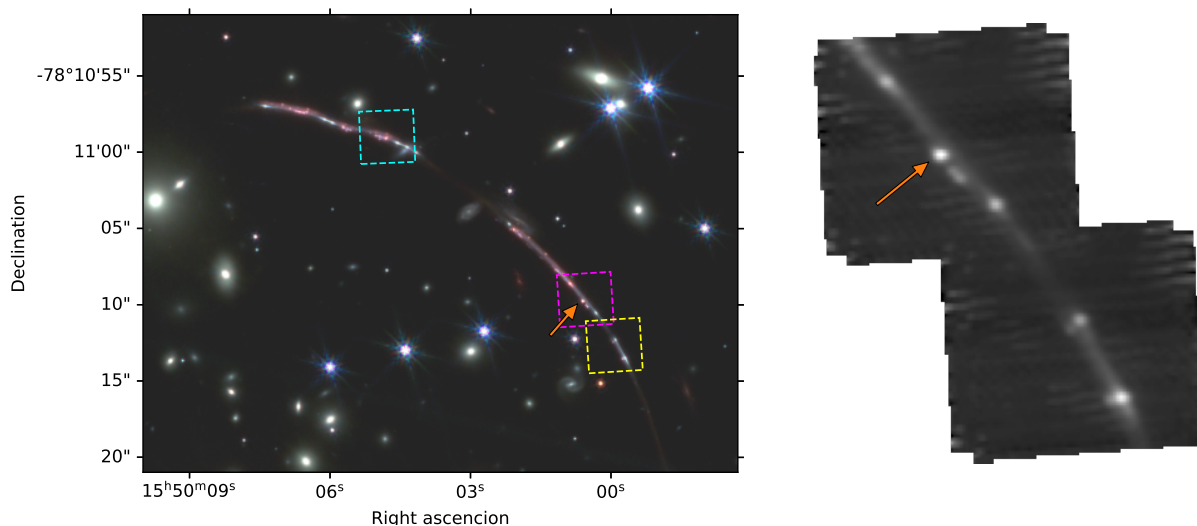


**Fig. 1.** (left) Overview of the north and northwest arc with the NIRSpect IFU pointings overlaid. Cyan, magenta, and yellow squares depict pointing 1, 2, and 3, respectively. We used NIRCcam F115W, F200W and F444W filters for R,G,B, respectively. Godzilla in pointing 2 is marked with an orange arrow. (right) Pointing 2 and 3 showing Godzilla marked with an orange arrow. The images are oriented such that N is up, E is left; each combined NIRSpect pointing is approximately  $3'' \times 5$  on each side.

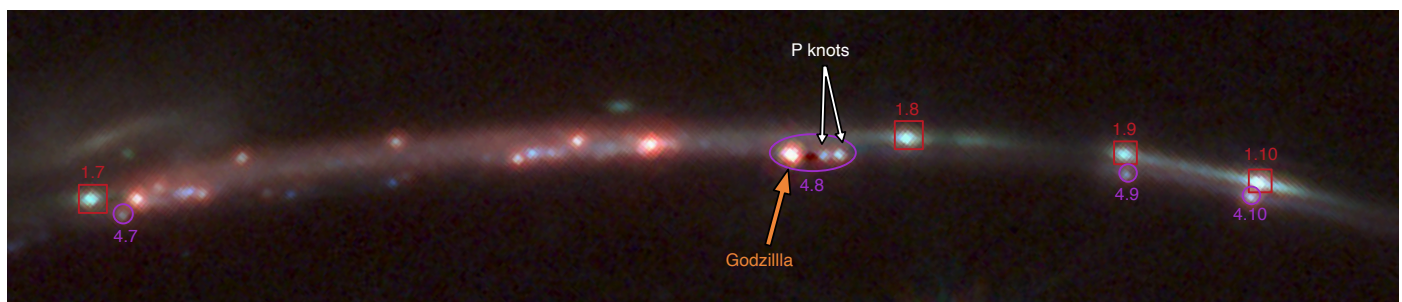


**Fig. 2.** The composite of NIRCcam F115W, F200W and F444W images of the northwest arc of the Sunburst Arc. Images 7 - 10 of clump 4 are marked with purple circles, while images 7 - 10 of the LyC leaking clump (clump 1) are marked with red squares. In image 8 of clump 4 (4.8), we observe Godzilla and the P knots (the two small clumps). Note the similarity in color between the P knots and the less magnified images of clump 4, and the difference from Godzilla.

measured fluxes as error. We measured the flux in the NE and SE regions through the same procedure using only one Gaussian component, as additional components did not improve the fit here from visual inspection.

We found that the  $[\text{O II}]\lambda\lambda 3727, 3729$  doublet is distinctively red-shifted compared to other lines (Figure A.1). To accurately recover the flux and flux ratio of the  $[\text{O II}]\lambda\lambda 3727, 3729$  doublet, we allowed the redshift of these lines to vary, but kept the distance between the two lines fixed. At Center, the narrow component of  $[\text{O II}]\lambda\lambda 3727, 3729$  doublet is offset relative to  $[\text{O III}]$  (and to nearby higher-order Balmer lines) by rest-frame  $1.73 \pm 0.6 \text{ \AA}$  ( $140 \pm 50 \text{ km s}^{-1}$ ). The broad component has a small offset consistent with 0 within the error bars.

In addition to a narrow and broad component, we found that a third, very broad component was necessary to obtain a good fit of  $\text{H}\alpha$  at the Center, NE, and SE regions. We found no sign that this extra component was needed to obtain good fits for  $[\text{O III}]\lambda\lambda 4960, 5008$ . Figure 5 clearly shows the necessity of the very broad component in fitting  $\text{H}\alpha$ . The narrow and broad components of the  $[\text{N II}]\lambda\lambda 6550, 6585$  doublet were set to have fixed ratios of 1:2.96 (Tachiev & Fischer 2001). In our spectra, there are a few more doublets arising from the same upper level, which thus have fixed flux ratio (e.g.  $[\text{O III}]\lambda\lambda 4960, 5008$ ,  $[\text{N III}]\lambda\lambda 3870, 3969$ ,  $[\text{O I}]\lambda\lambda 6302, 6366$ ), but we do not fix the flux

ratio of these doublets. The two-Gaussian model is a simplification of the true line shape, and we found that additionally locking the line ratios led to over-constrained and over-simplified models producing poor fits. Allowing the line ratio to deviate slightly from the fixed value led to more accurate and better constrained models. The  $[\text{N II}]\lambda\lambda 6550, 6585$  doublet is the only exception from this, since  $[\text{N II}]\lambda 6550$  is completely buried in the very broad component of  $\text{H}\alpha$  and there is a chance of overestimating this broad component if we do not force the  $[\text{N II}]\lambda 6550$  flux to be  $\sim 1/3$  of the  $[\text{N II}]\lambda 6585$  flux. Figure 6 shows the fits of  $\text{H}\alpha$  and  $[\text{N II}]\lambda\lambda 6550, 6585$  with the third, very broad  $\text{H}\alpha$  component included. In the NW and SW regions, the fits of the very broad component of  $\text{H}\alpha$  had fluxes consistent with 0, so we do not include this third component for  $\text{H}\alpha$  in these regions.

### 3.3. Dust reddening

We modeled dust attenuation using a starburst attenuation law (Calzetti et al. 2000), assuming a standard  $R_V = 4.05$ . We determined  $E(B-V)$  using  $\text{H}\alpha$ ,  $\text{H}\beta$ ,  $\text{H}\delta$ ,  $\text{H}8$ ,  $\text{Pa}9$ , and  $\text{Pa}10$ .  $\text{H}\gamma$  has not been included since it partially lies on the detector gap, making its measured flux unreliable. We also do not include  $\text{H}7$  as this line is blended with  $[\text{Ne III}]\lambda 3969$ . Intrinsic fluxes of Balmer and Paschen lines are calculated with PyNeb version 1.1.17 (Lurid-

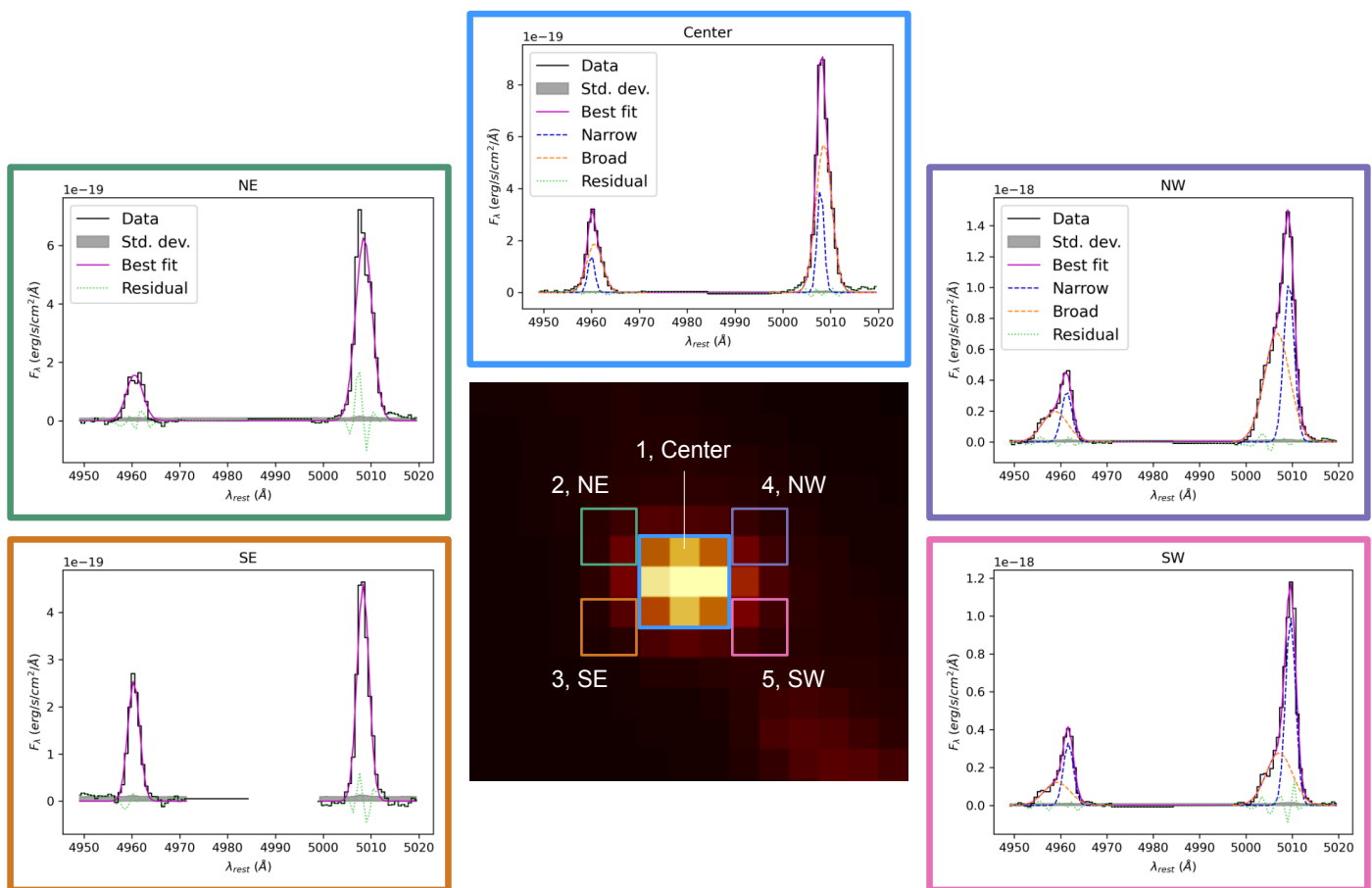


**Fig. 3.** The 5 regions where spectra have been extracted and their [O III] $\lambda\lambda 4960,5008$  doublet line profiles in the G140H/F100LP grating. The center figure shows the wavelength-axis median image of the NIRSPEC G140H/F100LP grating at the area of Godzilla. Two component (Center, NW, SW) and one component (NE, SE) Gaussian fits are also shown.

iana et al. 2015) assuming  $T_e = 10^4$  K and  $n_e = 10^3$  cm $^{-3}$ . We derived  $E(B - V)$  from each of the lines listed above, and subsequently computed an error-weighted average (Figure 7). When averaging  $E(B - V)$ , we excluded the very broad component of H $\alpha$  for Center, NE, and SE regions, as including it consistently produced a higher value of  $E(B - V)$  from H $\alpha$  than from the other lines. We note that there is a systematic uncertainty of  $\sim 5.5 - 7.5$  % in extinction-corrected flux that has not been included in the process of reddening correction. This uncertainty will affect all lines in a similar manner, and will therefore have a modest impact on derived line ratios.

## 4. Results

In this section, we focus mainly on kinematics and gas properties of the Center region. When deriving gas properties, we use PyNeb version 1.1.17 for electron temperature and density diagnostics.

### 4.1. Line identification

We have detected 57 rest-optical emission lines (Table 1 and Table 2), including auroral lines of four species (Figure 4). Contrary to previous observations that reported an absence of Balmer lines (Vanzella et al. 2020), we detected plentiful Balmer and Paschen lines with S/N of up to  $\sim 140$ . Interestingly, we detected a very strong permitted O I  $\lambda 8449$ . This line has been reported in Strom et al. (2023) from the stacked spectrum of  $z \sim 1 - 3$

galaxies, which they described as unexpected, since metal recombination lines usually are too weak and hardly detected even in local galaxies. Our detection is the first from the spectrum of a single object at such a high redshift. We will discuss this line in Section 4.4 and Section 5.3. In Table 1 and Table 2, we list all emission lines and their flux at Center, normalized by the total flux of H $\beta$ . In this paper, we only use the total flux of each line, deferring component-by-component analysis to future work.

### 4.2. Kinematics at Center

As described in Section 3.2, we computed kinematic properties from the [O III] $\lambda\lambda 4960,5008$  lines, summarized in Table 3. We find a redshift for the narrow component of the [O III] doublet of  $z_{\text{neb}} = 2.36983 \pm 0.00003$ , averaged from the two gratings (see Table 3). This is slightly blue-shifted compared to the value of 2.37025 reported by Mainali et al. (2022), which has been measured from [O III] $\lambda 5008$ . However, Mainali et al. used ground-based spectra, integrating and averaging over a larger area of the sky. IFU velocity maps (Rivera-Thorsen et al. 2024, in prep.) show that Godzilla is blue-shifted relative to the systemic redshift.

In the G140H/F100LP grating, the narrow and broad component showed full width at half maximum (FWHM) of  $37 \pm 26$  km s $^{-1}$  and  $216 \pm 6$  km s $^{-1}$ , respectively. In the G235H/F170LP grating, the FWHMs of the narrow and broad components were  $110 \pm 22$  and  $304 \pm 35$  km s $^{-1}$ . These are values corrected for the instrumental resolution. We suspect that the discrepancy in

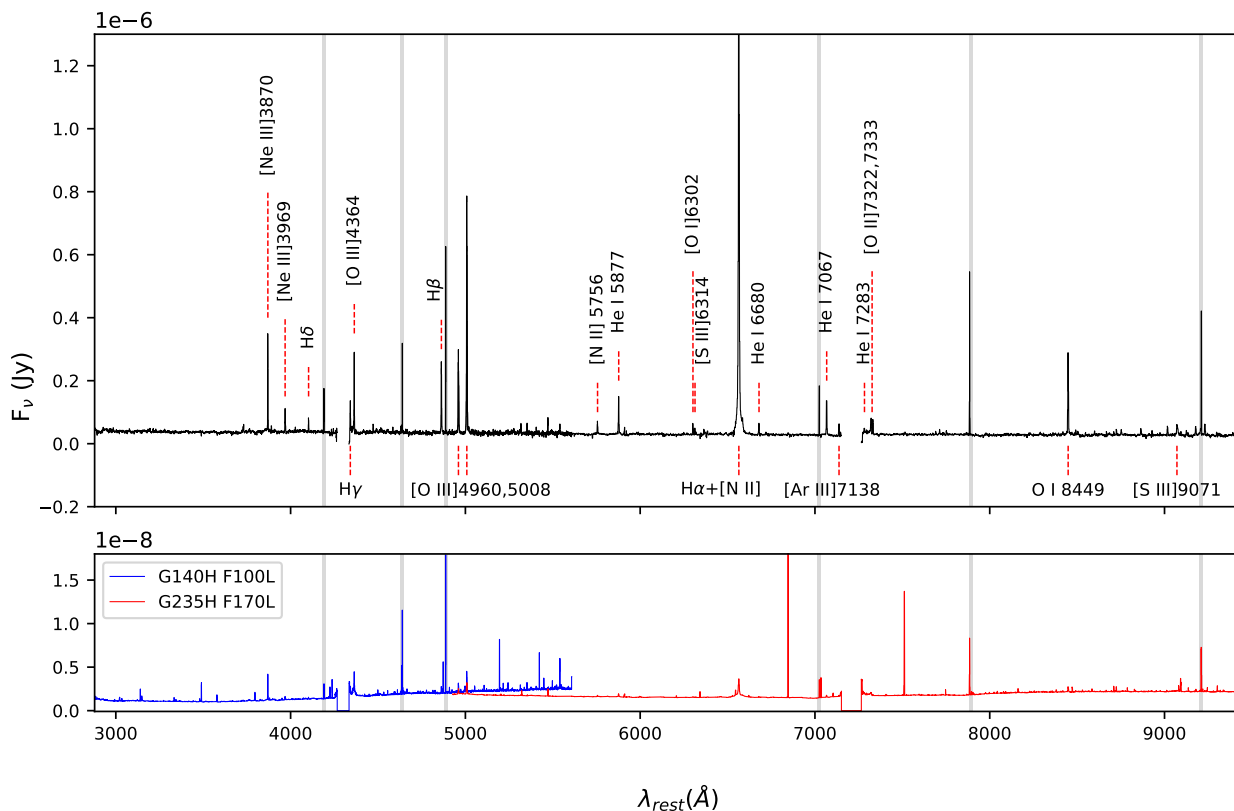


**Fig. 4.** (top) One dimensional spectrum extracted from the Center region, labeled with prominent lines. (bottom) Corrected error from G140H/F100LP and G235H/F170LP gratings shown in blue and red, respectively. Noise pixels are marked with grey shades. Both flux density and errors from the two gratings are overlapped in  $\sim 4925 - 5610 \text{ \AA}$ . See Figure A.1 and Figure A.2 for more detailed features.

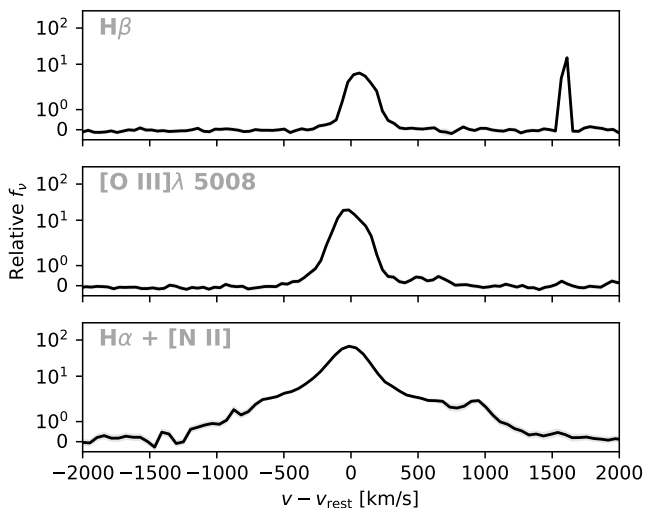


**Fig. 5.** Line profiles of  $H\beta$ ,  $[O \text{ III}]\lambda 5008$ , and  $H\alpha + [N \text{ II}]$  of the Center region, highlighting the broad component present in  $H\alpha$  but not the other lines. The y-axis scale is linear between -1 and 1, and logarithmic outside this interval. The velocity scale in the lower panel is centered around  $H\alpha$ .

FWHM between the two gratings is the result of the poorer resolution of the G235H grating, and possibly from inaccuracies in

the dispersion calibration files, which are all pre-flight. Although the FWHM is different in the two gratings, the measured fluxes of  $[O \text{ III}]\lambda\lambda 4960,5008$  are consistent within a few percent (Table 1, 2). A very broad component observed in  $H\alpha$  is blue-shifted by  $43 \pm 14$  and  $83 \pm 14 \text{ km s}^{-1}$  relative to the narrow and the broad component at the rest-frame ( $z_{\text{very broad}} = 2.36929 \pm 0.00015$ ), and has a large FWHM of  $547 \pm 31 \text{ km s}^{-1}$ . We found no evidence of an ongoing eruption. First, there is no clear P Cygni profiles in hydrogen and helium lines. Moreover,  $H\alpha$  at Center showed a maximum velocity of  $\sim 1200 \text{ km s}^{-1}$  (Figure 5) which is an order of magnitude smaller than the maximum velocity of  $H\alpha$  observed in  $\eta$  Car during Great Eruption ( $\sim 10^4 \text{ km s}^{-1}$ , Smith et al. 2018).

#### 4.3. Temperature and density diagnostics

We have detected auroral lines from four species:  $[N \text{ II}]\lambda 5756$ ,  $[O \text{ II}]\lambda\lambda 7322,7332$ ,  $[O \text{ III}]\lambda 4363$ , and  $[S \text{ III}]\lambda 6314$ . We note that the auroral line of  $[O \text{ III}]\lambda 4363$  is unusually high. As density diagnostics, we use  $[O \text{ II}]\lambda\lambda 3727,3730$  and  $[S \text{ II}]\lambda\lambda 6718,6733$ , but the S/N of  $[S \text{ II}]\lambda 6718,6733$  is too low in some regions, including Center. As temperature diagnostics, we use  $[O \text{ II}]\lambda\lambda 3727,3730/[O \text{ II}]\lambda\lambda 7322,7332$ ,  $[N \text{ II}]\lambda 5756/[N \text{ II}]\lambda\lambda 6550,6585$ ,  $[S \text{ III}]\lambda 6314/[S \text{ III}]\lambda 9071$ , and  $[O \text{ III}]\lambda\lambda 4363/[O \text{ III}]\lambda\lambda 4960,5008$ .

At Center, PyNeb fails to find a convergent density and temperature solution using the observed diagnostics. Figure 8 clearly

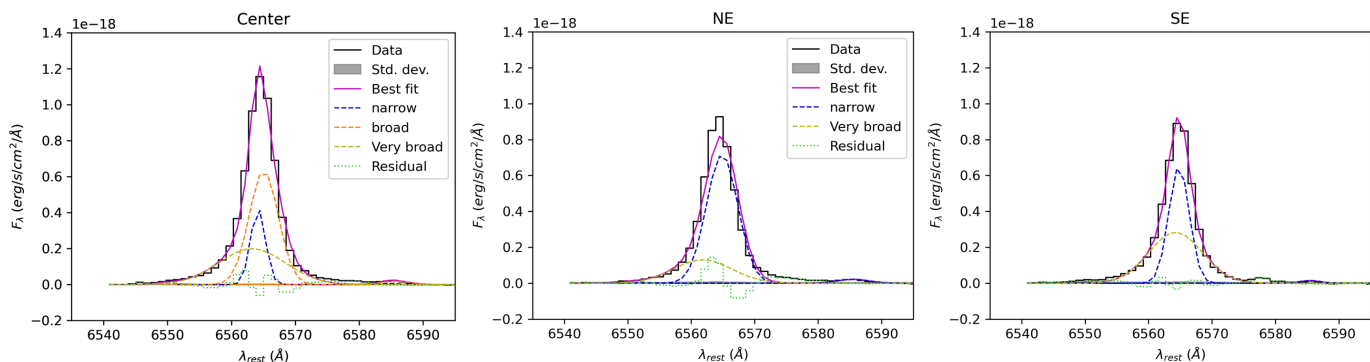


**Fig. 6.** Fitting result of  $H\alpha$  including a very broad component additional to default two component (Center) and one component (NE, SE) Gaussian profiles.

**Table 1.** Dust-corrected line fluxes for the Center G140H/F100LP spectrum.

#	Line	$\lambda_{\text{vac}} [\text{\AA}]^b$	$F(\lambda)/F(H\beta) [\%]^a$				S/N <sup>c</sup>
			Narrow	Broad	Total	Total (ext. corr.)	
1	H14	3723.00	2.8±0.7	0.5±0.9	3.3±0.5	5.6±0.8	7
2	[O II] 3727	3727.09	4.1±1.6	7.0±2.9	11.2±2.4	19±4	4.7
3	[O II] 3730	3729.88	8.3±2.1	4.0±3.4	12.2±2.4	21±4	5.0
4	[Ne III] 3870	3869.86	95.1±1.9	47.4±1.3	142.5±1.4	222.7±2.1	105
5	H8	3890.17	6.5±0.4	0.0±0.4	6.5±0.4	10.0±0.6	17
6	[Ne III] 3969	3968.59	19.4±0.8	16.4±1.2	35.8±0.6	53.3±0.9	58
7	H7	3971.20	4.6±0.6	1.5±0.9	6.1±0.6	9.0±0.9	10
8	He I 4027	4027.33	4.5±0.5	0.2±0.5	4.7±0.4	6.7±0.6	12
9	H- $\delta$	4102.90	10.6±0.6	7.5±0.9	18.0±0.5	25.1±0.7	35
10	H- $\gamma$	4341.69	16.0±1.0	31.7±1.4	47.7±0.9	59.3±1.1	56
11	[O III] 4364	4364.44	65.1±1.4	14.6±1.6	79.6±1.1	98.0±1.3	74
12	Fe II 4418	4418.07	2.3±0.5	0.4±0.6	2.7±0.4	3.2±0.5	6
13	[Fe II] 4453	4453.35	1.6±0.4	0.00±0.14	1.6±0.4	1.8±0.4	4.4
14	He I 4473	4472.73	6.4±0.6	1.9±0.9	8.3±0.6	9.8±0.7	15
15	Fe II 4490	4490.44	2.4±0.4	0.0±0.5	2.4±0.5	2.8±0.5	5
16	Fe II 4493	4492.67	0.00±0.2	4.5±0.6	4.5±0.6	5.2±0.7	8
17	Fe II 4557	4557.17	2.2±0.5	0.8±0.8	3.0±0.5	3.4±0.6	6
18	Fe II 4585	4585.12	4.7±0.6	0.8±0.8	5.5±0.5	6.1±0.6	10
19	Fe II 4631	4630.64	4.6±0.4	0.00±0.19	4.6±0.4	5.0±0.4	12
20	[Fe III] 4659	4659.35	2.9±0.6	0.7±0.8	3.6±0.5	3.9±0.6	7
21	H- $\beta^d$	4862.69	25.8±0.7	74.2±1.1	100.0±0.7	100.0±0.7	143
22	[O III] 4960	4960.30	26.7±0.8	81.9±1.1	108.5±0.7	104.5±0.7	146
23	[O III] 5008	5008.24	76±1	250±2	326±1	308±1	344
24	Fe II 5017	5016.92	1.5±0.7	5.3±1.1	6.8±0.7	6.4±0.6	10
25	Fe II 5020	5019.84	1.8±0.6	2.8±1.0	4.6±0.7	4.4±0.7	7

**Notes.**

<sup>(a)</sup> Line fluxes are normalized by the total best-fit flux of  $H\beta$ , but not including its uncertainty.

<sup>(b)</sup> Wavelengths from the NIST Atomic Spectral Database (Kramida & Ralchenko 1999).

<sup>(c)</sup> Signal-to-noise of the total, measured (uncorrected) line flux; rounded off to nearest integer unless where lower than 5.

<sup>(d)</sup>  $F(H\beta)_{\text{obs}} = 3.216 \pm 0.022 \times 10^{-18}$ ,  $F(H\beta)_{\text{corr}} = 2.156 \pm 0.015 \times 10^{-17}$  (erg/s/cm<sup>2</sup>/Å).

shows that density and temperature diagnostics are probing different gas phases. To explain the observed ratios of the auroral [O III] $\lambda\lambda 4363$ , [S III] $\lambda 6314$ , and [N II] $\lambda 5756$  lines to their nebular counterparts, the gas should have density of  $\geq 10^6 \text{ cm}^{-3}$ . The density range probed by [O II] $\lambda\lambda 7322, 7332$  extends down to  $\sim 10^4 - 10^5 \text{ cm}^{-3}$ , but still does not converge with the density solution from [O II] $\lambda\lambda 3727, 3730$  of  $\lesssim 10^3 \text{ cm}^{-3}$ . We emphasize that the narrow component of [O II] $\lambda\lambda 3727, 3730$  is redshifted by  $140 \pm 50 \text{ km s}^{-1}$  in the rest-frame compared to the narrow component of [O III] $\lambda\lambda 4960, 5008$ . [O II] $\lambda\lambda 3727, 3730$  might

have an origin different from other emission lines, and may not be suitable as a density diagnostic. Previous observations found that the UV density diagnostic lines C III] $\lambda\lambda 1907, 1909$  and Si III] $\lambda\lambda 1883, 1892$  suggest a very high density of  $n_e \geq 10^6 \text{ cm}^{-3}$  (Vanzella et al. 2020) in Godzilla. One of the main reasons for this discrepancy is that collisionally excited [O II] and [S II] start to be suppressed at relatively lower density ( $n_{\text{crit}} \approx 4000 - 10^4 \text{ cm}^{-3}$ , Draine 2011) compared to other higher density tracers such as C III] (Kewley et al. 2019). We discuss this more in Section 5.2 and Section 5.3.1.

**Table 2.** Measured and dust corrected line fluxes for the Center G235H/F170LP spectrum.

#	Line	$\lambda_{\text{vac}}$ [Å]	F( $\lambda$ )/F(H $\beta$ ) [%]				S/N
			Narrow	Broad	Total	Total (ext. corr.)	
22	[O III] 4960	4960.30	39.3±1.5	77.1±1.8	116.4±0.9	112.1±0.8	137
23	[O III] 5008	5008.24	102.1±1.8	220.2±2.1	322.4±1.0	305.0±1.0	316
24	Fe II 5017	5016.92	1.1±1.5	6.1±2.3	7.3±1.1	6.9±1.0	7
25	Fe II 5020	5019.84	0.0±0.9	6.0±1.2	6.0±1.1	5.6±1.0	6
26	[N II] 5756	5756.19	10.4±0.7	2.2±1.0	12.7±0.5	9.31±0.35	27
27	He I 5877	5877.25	25.0±0.8	13.7±1.0	38.7±0.5	27.4±0.4	76
28	[O I] 6302	6302.05	7.1±0.5	3.4±0.7	10.5±0.4	6.69±0.24	28
29	[S III] 6314	6313.81	4.6±0.5	0.7±0.6	5.3±0.4	3.36±0.23	15
30	[O I] 6366	6365.54	2.9±0.5	1.5±0.7	4.4±0.4	2.76±0.24	11
31	Si II 6373	6373.13	0.6±0.5	2.1±0.7	2.7±0.4	1.66±0.23	7
32	[N II] 6550	6549.86	0.71±0.01	3.85±0.11	4.56±0.12	2.70±0.07	37
33	H- $\alpha$ <sup>†</sup>	6564.63	128±4	380±12	509±16	300±9	32
	H- $\alpha$ <sup>‡</sup>	6564.63	—	—	781±9	—	—
34	[N II] 6585	6585.28	2.10±0.04	11.40±0.33	13.5±0.4	7.93±0.22	37
35	He I 6680	6679.99	6.5±0.5	2.2±0.6	8.74±0.35	5.01±0.20	25
36	[S II] 6718	6718.29	$(4 \pm 2) \times 10^{-4}$	1.6±0.3	1.6±0.3	0.9±0.2	4.7
37	[S II] 6733	6732.67	0.66±0.23	0.00±0.04	0.66±0.23	0.37±0.13	2.9
38	He I 7067	7067.14	17.1±0.4	12.2±0.6	29.27±0.35	15.27±0.18	83
39	[Ar III] 7138	7137.76	5.4±0.4	3.0±0.6	8.4±0.4	4.29±0.18	23
40	He I 7283	7283.36	2.58±0.34	0.0±0.4	2.60±0.32	1.29±0.16	8
41	[O II] 7322	7322.01	7.7±0.5	2.3±0.6	10.0±0.4	4.94±0.18	27
42	[O II] 7333	7332.75	7.88±0.26	0.00±0.19	7.88±0.25	3.88±0.12	32
43	[Ar III] 7753	7753.19	1.60±0.31	0.4±0.4	1.98±0.28	0.90±0.13	7
	O I 7776	7776.31	0.04±0.13	0.00±0.05	0.04±0.14	0.02±0.06	0.3
44	O I 7990	7989.17	0.60±0.22	0.00±0.10	0.60±0.22	0.26±0.10	2.7
45	Pa17	8469.58	0.64±0.24	0.00±0.20	0.64±0.23	0.25±0.09	2.8
46	O I 8449	8448.68	26.8±0.4	25.0±0.6	51.8±0.4	20.75±0.15	139
	O I 8449*	8448.68	—	—	47.8±0.4	—	134
	Fe II 8453	8453.34	$(3 \pm 6) \times 10^{-5}$	$(3 \pm 2) \times 10^{-4}$	$(3 \pm 2) \times 10^{-4}$	$(1.3 \pm 0.7) \times 10^{-4}$	1.8
	Fe II 8453*	8453.34	—	—	3.02±0.26	—	12
47	Fe II 8490	8492.44	1.71±0.34	0.8±0.5	2.47±0.33	0.98±0.13	8
	Fe II 8490*	8492.44	—	—	2.58±0.26	—	10
48	Pa16	8504.82	0.76±0.32	1.0±0.5	1.74±0.33	0.69±0.13	5
49	Pa15	8547.73	0.97±0.28	0.2±0.4	1.14±0.28	0.45±0.11	4.1
50	Pa14	8600.75	1.63±0.25	0.00±0.25	1.63±0.24	0.64±0.10	7
51	Pa13	8667.40	0.60±0.24	0.00±0.24	0.60±0.24	0.23±0.09	2.5
52	Pa12	8752.88	1.41±0.32	1.8±0.5	3.19±0.32	1.22±0.12	10
53	Pa11	8865.22	1.72±0.31	2.4±0.5	4.07±0.31	1.53±0.12	13
54	Pa10	9017.38	2.50±0.30	2.2±0.5	4.72±0.30	1.74±0.11	16
55	[S III] 9071	9071.09	0.000±0.03	9.0±0.3	9.0±0.3	3.3±0.1	28
56	[Cl II] 9126	9126.10	1.32±0.25	0.4±0.4	1.67±0.27	0.61±0.10	6
57	Pa9	9231.55	3.32±0.29	2.7±0.4	6.07±0.30	2.17±0.11	20

**Notes.** Column description and notes in Table 1 also apply here.

<sup>(†)</sup> H $\alpha$  line fitted with a third, very broad component, but the Total flux reported here is not including that; see next row.

<sup>(‡)</sup> Total flux of H $\alpha$  including the third, very broad, Gaussian component.

<sup>(\*)</sup> Narrow, fluorescence-pumped lines re-fitted with only one Gaussian component and relaxed line width. See more in Section 5.3.2.

#### 4.4. Bowen fluorescent lines

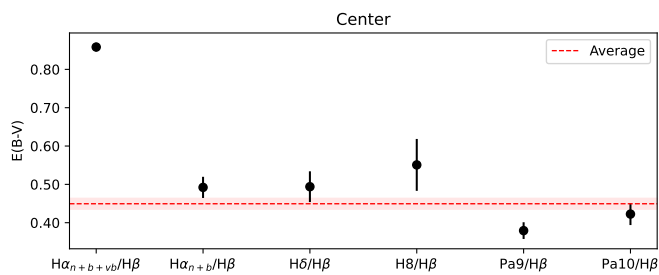
As reported in Section 4.1, we detect a strong O I  $\lambda$ 8449 line at Center, which has flux that is  $20.75 \pm 0.15$  % of the H $\beta$  flux, with S/N  $\approx$  139. We believe this line has mainly arisen from photo-excitation by accidental resonance (PAR) due to Ly $\beta$  photons, as suggested in Johansson & Letokhov (2005) and as reported for Ly $\alpha$ -pumped lines in Vanzella et al. (2020). We disfavor other mechanisms, such as recombination, collisional excitation, or pumping by stellar continuum, considering very weak or absent

O I  $\lambda$ 7776 and O I  $\lambda$ 7990, and the detection of rest-UV O I emission lines arising from PAR.

Figure 9 shows various O I lines in the rest-frame UV (*a*, *b*) and optical (*c*, *d*) wavelength. Panel *c* shows an absence of the O I  $\lambda$ 7776 triplet and O I  $\lambda$ 7990 complex. Measuring the ratio between O I  $\lambda$ 7776/ $\lambda$ 8449 yields a  $3\sigma$  upper limit of 0.009. This is inconsistent with the first two scenarios, since we expect  $\lambda$ 7776/ $\lambda$ 8449  $\approx$  1.7 and  $\lambda$ 7776/ $\lambda$ 8449  $\approx$  0.3 for the case of recombination and collisional excitation, respectively (Grandi 1980; Haisch et al. 1977). The line ratio O I  $\lambda$ 7990/ $\lambda$ 8449 is ex-

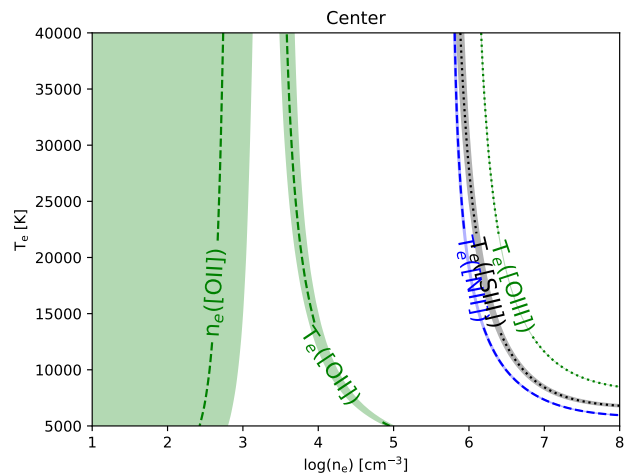
**Table 3.** Kinematics information for all regions. NE and SE regions only have narrow component since we did one component Gaussian fitting for these regions.

	$z$			FWHM [ $\text{km s}^{-1}$ ]		
	Narrow	Broad	Very broad ( $\text{H}\alpha$ )	Narrow	Broad	Very broad ( $\text{H}\alpha$ )
<b>(G140H/F100LP)</b>						
Center	$2.36976 \pm 0.00004$	$2.37022 \pm 0.00003$	—	$37 \pm 26$	$216 \pm 6$	—
NE	$2.37017 \pm 0.00003$	—	—	$227 \pm 7$	—	—
SE	$2.37005 \pm 0.00002$	—	—	$152 \pm 4$	—	—
NW	$2.37070 \pm 0.00002$	$2.36897 \pm 0.00008$	—	$132 \pm 8$	$376 \pm 8$	—
SW	$2.37094 \pm 0.00002$	$2.36930 \pm 0.00016$	—	$126 \pm 7$	$389 \pm 18$	—
<b>(G235H/F170LP)</b>						
Center	$2.36990 \pm 0.00004$	$2.37029 \pm 0.00013$	$2.36929 \pm 0.00015$	$110 \pm 22$	$304 \pm 35$	$547 \pm 31$
NE	$2.37012 \pm 0.00003$	—	$2.36855 \pm 0.00053$	$239 \pm 8$	—	$478 \pm 72$
SE	$2.37009 \pm 0.00003$	—	$2.36981 \pm 0.00006$	$126 \pm 9$	—	$435 \pm 16$
NW	$2.37064 \pm 0.00003$	$2.36903 \pm 0.00009$	—	$93 \pm 16$	$380 \pm 9$	—
SW	$2.37090 \pm 0.00002$	$2.36918 \pm 0.00013$	—	$92 \pm 11$	$396 \pm 14$	—


**Fig. 7.**  $E(B - V)$  as computed from the strongest Balmer and Paschen lines for the Center region. The value from  $\text{H}\alpha$  is shown both including and excluding the very broad component. Similar figures for the surrounding regions are shown in Figure B.1.

pected to have a value of  $\lambda 7990/\lambda 8449 \approx 0.052$  from the continuum fluorescence cascade calculation by Grandi (1980) (assuming case B recombination and  $T_e = 10^4$  K). This is inconsistent with the observed value  $0.013 \pm 0.005$  in Godzilla, by more than  $7\sigma$ , significantly weakening the stellar continuum excitation scenario. Assuming case A recombination, these ratios can become as low as 0.0030, but case A does not seem to be a proper assumption as we already know that there exists a dense gas component.  $\text{O I } \lambda 7256$  is another line emitted from the same stellar continuum excitation cascade, but it falls in the detector gap.

Moreover, we point out that the UV counterparts of Ly $\beta$ -pumped lines, the  $\text{O I } 1302.2, 1304.9, 1306.0$  triplet and  $\text{O I } \lambda 1641.31$  (Shore & Wahlgren 2010, see Figure 1) emission lines, are detected in the MagE spectrum, although 1304.9 is not obvious due to the effect of Si II absorption (Figure 9-a, b). The observation of these other Ly $\beta$ -pumped lines of the same cascade, as well as the absence of recombination lines and continuum-pumped lines, supports that the permitted  $\text{O I } \lambda 8449$  is a Ly $\beta$ -pumped line. Previously, emission near  $1640 \text{ \AA}$  was identified as He II  $\lambda 1640.42$  by Vanzella et al. (2020) and suggested as supporting evidence for a transient scenario. On the other hand, Diego et al. (2022) argued that it is  $\text{O I } \lambda 1641$  based on its line center. Taking into account that we have detected


**Fig. 8.** Temperature and density solutions from PyNeb for the spectrum extracted from the Center region in Figure 3. Oxygen, sulphur, nitrogen diagnostics are depicted in green, grey, and blue colors, respectively, with shades representing the  $1-\sigma$  confidence regions. We note that the  $T_e[\text{O II}]$  diagnostic shown here might not be trustworthy, if indeed the  $[\text{O II}] \lambda \lambda 3727, 3730$  emission has a different region of origin than its auroral counterpart (see Section 3.2, Section 4.3). Similar figures for the surrounding regions are shown in Figure B.2.

other Ly $\beta$ -pumped  $\text{O I}$  lines while not detecting any He II emission lines, we conclude that this emission is from  $\text{O I}$ .

We also report the detection of Ly $\alpha$ -pumped Fe II  $\lambda 8490$  with S/N of 8. Interestingly, the other Ly $\alpha$ -pumped line near this line, Fe II  $\lambda 8453$ , has not been detected. Discussion of the Bowen fluorescent lines will be continued in Section 5.3.

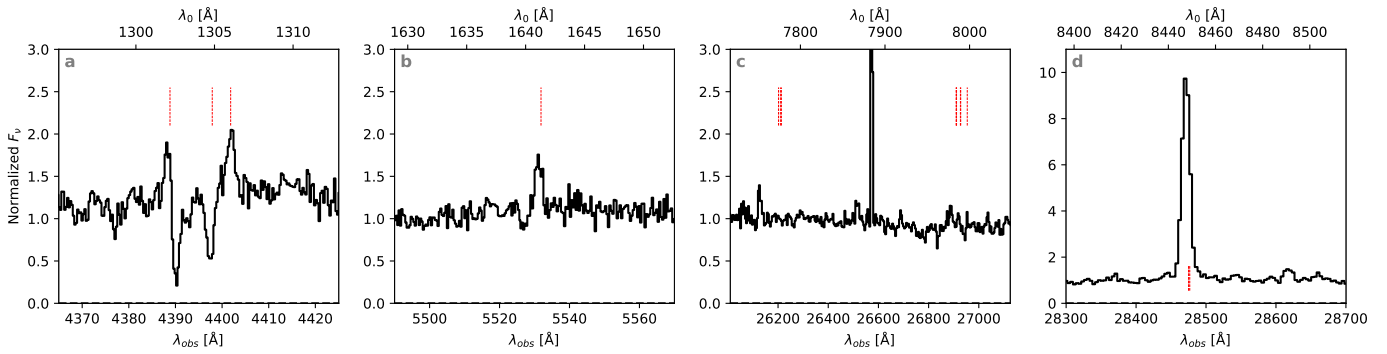


**Fig. 9.** *a, b:* Rest-frame UV spectrum of Godzilla from Magellan/MagE (Rigby et al. in prep.), showing the O I triplet and Si II line complex around 1304 Å and O I 1641 Å. All these O I lines are part of the Ly $\beta$  pumped Bowen fluorescence cascade. *c:* NIRSpec spectrum showing position of the rest-frame optical O I recombination lines and/or stellar continuum excitation cascade triplet around 7776 Å and line complex at around 7990 Å, where we would expect to see line emission if the observed O I cascade were due to recombination or stellar continuum pumping. *d:* Ly $\beta$ -pumped, Bowen fluorescent O I 8449 Å.

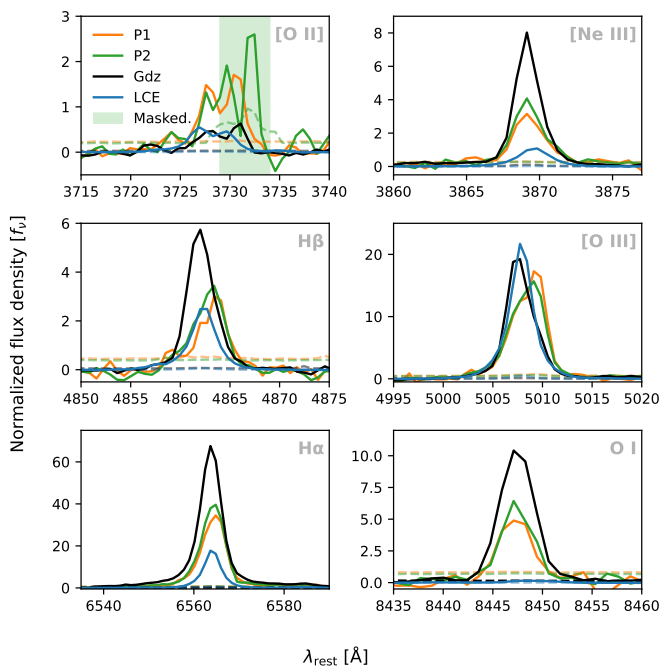


**Fig. 10.** Selected, relative line fluxes from Godzilla, the two *P*-knots, and for comparison the Lyman Continuum emitter (LCE) knot, highlighting kinematics and relative line strengths. The green shaded interval in the [O II] panel indicates where P2 suffers from contamination from noisy pixels. The spectra were first normalized by their median value, the continuum then subtracted, and the resulting lines all normalized by the integral of [O III] 5008 of each spectrum.

## 5. Discussion

### 5.1. Constraints from the NIRC*am* imaging and lensing models

The NIRC*am* data strengthens the extreme magnification scenario suggested by Diego et al. (2022) and Sharon et al. (2022). Figure 2 shows the April 2023 NIRC*am* observation, and Godzilla still maintains similar brightness to that of the Sunburst LCE (clump 1, marked with red squares). It expands the observed duration of Godzilla from previously 2 years to 5 years. While Diego et al. (2022) included the original discovery ESO New Technology Telescope (NTT) observations in 2014 (Dahle et al. 2016), we exclude this as there Godzilla is not

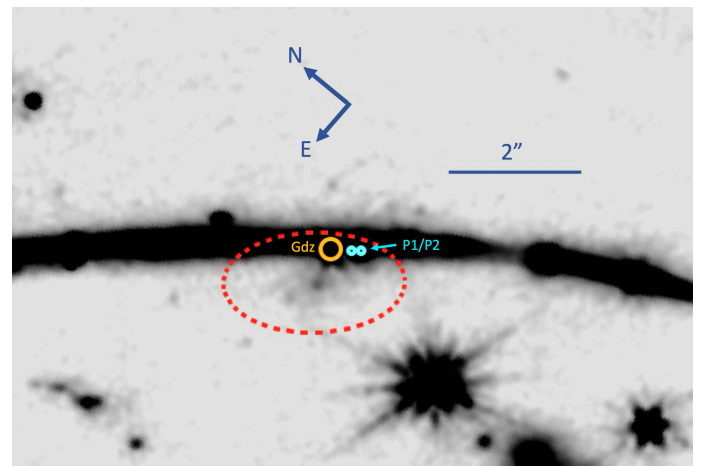


**Fig. 11.** Combined NIRC*am* F115W+F150W image, smoothed by a FWHM = 0.1'' Gaussian to bring out low surface brightness details. The dashed ellipsoid marks a low surface brightness galaxy close to Godzilla (larger circle) and the *P* knots (smaller circles).

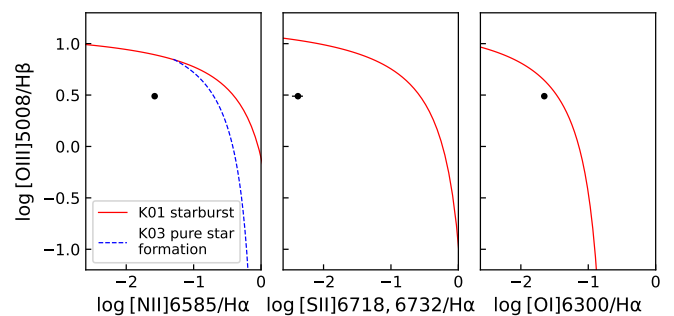


**Fig. 12.** N2, S2, O1 BPT diagram of Center (black dot with error bars). Theoretical maximum starburst (Kewley et al. 2001) and empirical star formation (Kauffmann et al. 2003) lines are shown in red solid and blue dashed lines respectively.

clearly resolved. Counting from the February 2018 HST observation, Godzilla has maintained its approximate luminosity for  $\sim 1.5$  years in the rest-frame.

Vanzella et al. (2020) argued that Godzilla (“Tr” in their terminology) is a Type II*n* SN, a type of SN with narrow lines in

their spectra. These narrow lines are believed to arise when a massive star explodes into a dense CSM. Although Type II<sub>n</sub> SNe can be observed more than a few decades after explosion (Immler et al. 2005; Milisavljevic et al. 2012), it does not mean that it maintains high luminosity for that long time. One sub-type of Type II<sub>n</sub> SNe, II<sub>n</sub>-P (Mauerhan et al. 2013), is a type that shows a lasting, luminous plateau phase. A recent theoretical work however predicted the duration of this plateau phase to around 100 days at most (Khatami & Kasen 2023). Thus, a luminous plateau lasting for at least 1.5 years observed in Godzilla is highly unlikely to happen in any kind of SN known so far.

Godzilla is also unlikely to be some other kind of rare transient that shows an approximately flat light curve for 1.5 years. As summarized in Section 1, such a scenario contradicts the maximum time delay predicted from the lens model by Sharon et al. (2022), as a sudden increase in luminosity should have been observed in counter images in other arcs. Godzilla and a pair of clumps next to it (the ‘‘P knots’’ following Diego et al. 2022) are believed to be nearby in the source plane (Diego et al. 2022), and the lens model from Sharon et al. (2022) predicts that Godzilla and the P knots are the highly resolved 8th counter-image of clump 4 (depicted with purple circle labeled ‘‘4.8’’ in Figure 2). Godzilla still appears only near the position of image 4.8, with brightness comparable to the LCE, while other images of clump 4 such as 4.3 and 4.4 in the north arc remain much fainter than the LCE. Non-detection of any sudden luminosity changes in or near other lensed images of clump 4 over 1.5 years rest-frame time domain tells us that the reason that Godzilla is uniquely observed near image 4.8 is because it is extremely magnified only at that position.

Such an extreme magnification can happen if Godzilla lies on the critical curve, as suggested in Diego et al. (2022). In Figure 10, we compared emission line profiles normalized by the flux of [O III]  $\lambda$ 5008 at each spectrum for the P knots, Godzilla and Sunburst LCE. The left and right clumps in the P knots, P1 and P2, show nearly identical line profile traits such as redshift, peak and the line width in various emission lines, and are clearly distinguished from Godzilla. It suggests that the P knots are likely to be the mirrored image of the same object different from Godzilla, and strengthens the hypothesis of a perturbing mass in the foreground generating a critical curve crossing the top of Godzilla and between the P knots (Diego et al. 2022, see Figure 6). The plausibility of this lensing scenario is strengthened by the NIRCcam detection of a low surface brightness galaxy centered only 0.5'' from Godzilla. As shown in Figure 11, this galaxy has a clumpy structure and may be responsible for creating the small-scale perturbations needed to shift the critical curve to the locations suggested by Diego et al. (2022).

Figure 10 also shows that Godzilla and the P knots present strong O I  $\lambda$ 8449 compared to [O III]  $\lambda$ 5008 which is a rare characteristic clearly distinctive from the LCE. This again supports various lens models that predicted Godzilla and the P knots are in close vicinity in the source plane. We propose that Godzilla is a small object dominated by one or a few stellar sources, located at the outskirts of clump 4. The color of other counterimages of clump 4 such as 4.9 and 4.10 (Figure 2) also supports this idea. The color of image 4.9 and 4.10 and the P knots, which may be images of clump 4, is bluer than Godzilla. Future lens model analysis will quantitatively discern these theories. For the rest of this paper, we assume that Godzilla is much smaller than a star cluster, which is already implied by its much larger magnification factor compared to other clumps.

**Table 4.** Computed color excess ( $E(B - V)$ ) for the 5 regions.

	$E(B - V)$
Center	$0.45 \pm 0.01$
NE	$0.78 \pm 0.04$
SE	$0.77 \pm 0.03$
NW	$0.24 \pm 0.02$
SW	$0.25 \pm 0.03$

## 5.2. Spatial analysis

As seen in Table 3, the broadest component at Center, NE, and SE regions show a high value of FWHM  $\sim 435$ – $547$  km s<sup>-1</sup>. It is larger than the expansion velocity of most local LBVs (a few to 100 km s<sup>-1</sup>), and similar to that of  $\eta$  Car (Weis & Bomans 2020). While NW and SW regions do not have the very broad component in H $\alpha$ , these regions show strong outflow features in many lines. In the G140H/F100L grating, NW and SW regions show broad components blue-shifted compared to the narrow component by  $143 \pm 8$  km s<sup>-1</sup> and  $153 \pm 12$  km s<sup>-1</sup> in the rest-frame, respectively.

One distinguishing feature of Godzilla is that it is very dusty. The Sunburst Arc is in general not so dusty (Mainali et al. 2022). The dust cover in this region seems extremely uneven; in the spatial dust map of the whole Sunburst Arc, Godzilla and counter-images of clump 4 stand out with a significantly higher  $E(B - V)$  than typical values for the galaxy (Rivera-Thorsen et al. 2024, in prep.). As shown in Table 4, the  $E(B - V)$  reaches  $\sim 0.24$ – $0.78$ , depending on the region. The NW and SW regions, where strong outflow features are observed (Figure 3), are less dusty. Interestingly, Mainali et al. (2022) find that their MagE spectrum containing Godzilla have a slightly lower  $E(B - V)$  compared to other regions based on the H $\alpha$ /H $\beta$  Balmer decrement (0.02 for the M-3 pointing containing Godzilla vs. 0.04–0.15 for the other pointings). We cannot say with certainty what causes this discrepancy, but speculate that it might be an effect of atmospheric blurring and the much larger aperture area of the MagE slit compared to the extraction aperture used here.

The surrounding regions are also variant in their gas temperature and density. Looking at the temperature and density diagnostics diagram in the surrounding regions (Figure B.2), we can see that the density is higher ( $n_e \gtrsim 10^3$  cm<sup>-3</sup>) in the SE and SW regions compared to the NE and NW regions ( $n_e < 10^3$  cm<sup>-3</sup>). The cross section of the density diagnostics and low temperature diagnostic line ([O II]  $\lambda$ 7322,7332) is also more biased to the higher density in the SE and SW regions.

Spatially variant kinematics, dust properties, and gas temperature and density clearly show that the central bright source is surrounded by multi-phase, inhomogeneous gas. This circumstellar medium and dust might have been ejected through stellar winds or previous eruptions, which is a common feature of massive stars at the late, evolved stages of their short lives.

## 5.3. Comparison to Bowen fluorescent lines observed in $\eta$ Carinae

### 5.3.1. The Weigelt blobs

As mentioned in Section 4.3, we know that dense gas of  $n_e \gtrsim 10^6$  cm<sup>-3</sup> exists in the regions of Godzilla (Vanzella et al. 2020), although our optical density diagnostics only offer limited constraints on low density gas. Moreover, we have shown that the

strong, narrow permitted oxygen line O I  $\lambda 8449$  has most likely arisen from a Ly $\beta$  pumping mechanism (Section 4.4). Existence of high density gas and the strong fluorescent line emission is evocative of the Weigelt blobs in the  $\eta$  Car systems explained in Section 1. These dense gas condensations are mainly neutral and have an ionized surface layer facing the stars (See Figure 1. in Johansson & Letokhov 2005, for a sketched out overview). The O I in the neutral condensations is shielded by hydrogen from ionisation, but exposed to Ly $\beta$  photons emitted from the H II surface of the blob, as well as the stellar wind, populating the 3d<sup>3</sup>D level of the neutral oxygen atoms (Johansson & Letokhov 2005, Figure 4). This level has an excitation energy very close to the resonant energy of Ly $\beta$  photons and can be pumped by it, if Ly $\beta$  is sufficiently strong (PAR). Shore & Wahlgren (2010, Figure 1) show a different view of this same cascade. Once the 3d<sup>3</sup>D level is populated, it decays to 3p<sup>3</sup>P level through a  $\lambda = 11286$  Å transition which is outside the wavelength range of these observations. Subsequently, they continue to cascade down from 3p<sup>3</sup>P to 3s<sup>3</sup>S<sub>1</sub> through the  $\lambda = 8449$  Å transition, and from there into O I]  $\lambda 1641$  and the  $\lambda = 1302, 1304, 1306$  triplet. We note that all of these lines are strongly detected in the MagE and NIRSspec observations of Godzilla.

In the Weigelt blobs, as oxygen in the interior of the blob remains neutral, it results in a special situation where we observe strong Ly $\beta$ -pumped O I  $\lambda 8449$ , but not the recombination line O I  $\lambda 7776$ . The clear detection of the full Ly $\beta$ -pumped cascade, combined with the non-detection of O I  $\lambda 7776$  (Section 4.4, Figure 9) is the smoking gun that permitted O I lines in Godzilla has arisen from dense, Weigelt blob-like gas condensations.

### 5.3.2. A possible astronomical laser effect

Johansson & Letokhov (2005) discuss the possibility of astrophysical laser effects of O I  $\lambda 8449$  in the Weigelt blobs. As the decay of the lower 3s<sup>3</sup>S<sub>1</sub> level to the ground level is faster than the decay of the upper 3p<sup>3</sup>P level, population inversion occurs. O I  $\lambda 8449$  from Godzilla is due to Ly $\beta$  pumping, so we expect it to show an inverted population, but it does not necessarily mean that it is a laser since we cannot guarantee stimulated emission without information on the size of the blob and amplification of the O I  $\lambda 8449$  line. For observational confirmation, Johansson & Letokhov (2005) suggests looking for sub-Doppler width, i.e. the line width narrower than the width caused by Doppler broadening, of the  $\lambda 8449$  line.

Ly $\alpha$ -pumped iron lines can provide us an additional clue about the sub-Doppler width of the O I  $\lambda 8449$  line. Along with the Ly $\beta$ -pumped O I  $\lambda 8449$ , we detect Ly $\alpha$ -pumped Fe II  $\lambda 8490$  with S/N of 8 (see Table 2). Interestingly, another Ly $\alpha$ -pumped iron line, Fe II  $\lambda 8453$ , which arise from the same mechanism thus should appear is not detected in the fits using [O III]  $\lambda 4960, 5008$  as kinematic template (Table 2). This line is blended with O I  $\lambda 8449$ , and we suspect that its flux may have been included in the O I  $\lambda 8449$  flux since the O I  $\lambda 8449$  line is narrower than other lines. We fitted the fluorescent lines again, using only one component and relaxing the width constraint. The result is shown in Table 2 with asterisk. We measured FWHM of  $106 \pm 5$  km s<sup>-1</sup> for the fluorescent lines and it increased S/N of Fe II  $\lambda 8453$  from  $\sim 1.8$  to  $\sim 12$ . However, along with the lack of information on the thermal broadening in this object, the spectral resolution of NIRSspec does not allow sufficiently strong constraints on the line profile to confirm or falsify if the O I  $\lambda 8449$  emission observed in Godzilla is an astronomical laser.

### 5.3.3. Flux discrepancy in Ly $\alpha$ -pumped lines

The relative strengths of Ly $\alpha$ -pumped Fe II lines compared to the Ly $\beta$ -pumped O I  $\lambda 8449$  line is significantly smaller than observed in the Weigelt blobs (see Davidson & Humphreys 2012, Figure 5.4). In the Weigelt blobs, Fe II fluorescent lines are much stronger than O I  $\lambda 8449$ . This might imply an abundance difference, which is not surprising considering that Godzilla is at  $z = 2.37$  and the Weigelt blobs are in our Galaxy, where the metal enrichment has been enhanced by Type Ia SN. Several observations have already suggested significant alpha enhancement, i.e. iron deficiency, in  $z \sim 2 - 3$  galaxies (Steidel et al. 2016; Topping et al. 2020a,b; Cullen et al. 2021). Alternatively, it might be a circumstantial evidence of a O I laser and significant amplification in that line.

### 5.4. Constraints on the source energy

Emission lines give us information on the source temperature, and Godzilla does not seem to be extremely hot. We do not detect highly ionized lines such as He II or C IV. The property of the source would not be similar to a Very Massive Star, as we detect neither nebular nor broad stellar He II. Additionally, there is no sign of broad stellar C IV emission lines at 5808 Å, so this source would not be a Wolf-Rayet star. In Figure 12, we show the position of the object in the N2, S2, and O1 BPT diagrams of Center; it clearly falls within the stellar region, without any evidence for high-energy excitation or strong shocks, ruling out the intermediate-mass black hole (IMBH) scenario discussed in Diego et al. (2022).

An LBV is still a good explanation of what we observe, except the strong [Ne III]. The ionisation potential of doubly ionized neon (40.96 eV) might be a little too high for an LBV. In the Weigelt blobs, [Ne III] is only observed at times when the blob is exposed to the secondary star, which is hotter than the LBV star. The main stellar source in the Godzilla system might be a O4-O5 supergiant similar to the secondary star of  $\eta$  Car. But in that case, it is hard to explain the very dusty circumstellar medium and the existence of the dense gas blobs, which imply that main Godzilla component is an evolved massive star. Moreover, Diego et al. (2022) points out that hyperluminous stars are not as bright as LBVs and would require an unrealistically high magnification factor of  $\sim 5 \times 10^4$  which requires precise alignment of source and caustic that cannot be maintained more than a few weeks.

We can explain significant dust attenuation, strong Bowen fluorescent emission and [Ne III] emission line simultaneously if Godzilla is a binary system including a massive evolved star and a hotter star, analogous to  $\eta$  Car. It is a plausible scenario considering that 70% of massive stars are affected by binary interaction, and 50% have companions (Weis & Bomans 2020). It is also noteworthy that Smith & Tombleson (2015) and Smith (2019) suggested that LBVs result from close binary evolution. Alternatively, the properties listed above can be explained without invoking a binary scenario, if the gas condensations in Godzilla are exposed to more intense radiation of an LBV star compared to the Weigelt blobs. Assuming the LBV star has a similar temperature to  $\eta$  Car, this would be possible if the blobs were located more closely to the star than the Weigelt blobs. These two scenarios can potentially be discerned by observation of periodic variability of line emission.

## 6. Conclusions

We report the results from Cycle 1 JWST/NIRCam and NIRSpec observations of the object nick-named “Godzilla” in the Sunburst Arc. The Sunburst Arc is the brightest known gravitationally lensed galaxy at  $z = 2.37$  and consists of 12 full or partial images of the source galaxy. However, Godzilla only appears in one of these, despite being one of the brightest elements of that image. While the absence of counterimages of Godzilla has been explained with extreme magnification (Diego et al. 2022; Sharon et al. 2022), there is a still ongoing debate on the nature of the object (Vanzella et al. 2020; Pascale & Dai 2024). It has been suggested that Godzilla might be a rare stellar object called Luminous Blue Variable (LBV) based on the detection of uncommon Bowen fluorescent lines (Vanzella et al. 2020) and the luminosity constraints from the lens model (Diego et al. 2022). However, ground-based telescope observations from previous studies do not have a spatial resolution to test this at such a high redshift. In this work, we have extracted integrated spectra of Godzilla from NIRSpec IFU spaxels containing the central bright object (Center) and four regions (NE, SE, NW, SW) surrounding it (Figure 3), and measured the flux of emission lines using one to three component Gaussian profiles depending on the regions and lines. Our main findings are as follows:

1. We detected 57 emission lines from JWST/NIRSpec spectrum of the bright central region (Center), tabulated in Table 1 and Table 2. These include auroral lines of four species, and strong permitted  $O\text{I } \lambda 8449$ . This is the first detection of  $O\text{I } \lambda 8449$  from a single object outside the local universe (Figure 4) and implies unusual excitation mechanism other than ordinary recombination.
2. We showed that  $O\text{I } \lambda 8449$  is most likely produced through  $\text{Ly}\beta$ -pumping (Section 4.4), reporting the UV counterpart of the  $\text{Ly}\beta$ -pumped  $O\text{I}$  triplet detected in a Magellan/MagE spectrum, along with  $O\text{I} ]\lambda 1641$  (Figure 9). The presence of this  $\text{Ly}\beta$ -pumped cascade implies the existence of dense gas condensations in close vicinity of the energy source, which is analogous to the Weigelt blobs near Eta Carinae ( $\eta$  Car), an LBV star in Milky Way. We also discussed the hypothesized natural laser effect in  $O\text{I } \lambda 8449$ ; but while we find the suggestion plausible, we have not found basis in the data to confirm or refute a contribution to the line emission from such a natural laser (Section 5.3.2, 5.3.3).
3. NIRCam observations extend the baseline of observations of Godzilla to  $\sim 1.5$  years in the rest-frame; the source has an approximately flat light-curve over that time, and no counterimages have been detected, strengthening the case against the Type II<sub>n</sub> supernova scenario or any similarly short-lived transient event (Figure 2). Emission line profile comparison between Godzilla, the P knots (a pair of small clumps next to Godzilla) and the LCE (Figure 10) supports the microlensing scenario suggested by Diego et al. (2022). We suggest a newly detected low surface brightness galaxy near Godzilla (Figure 11) as a possible perturber creating the critical curve crossing on top of Godzilla. We concur that Godzilla only appears at its current position since it is extremely magnified, and that it is dominated by one or a few stellar sources (Section 5.1).
4. Godzilla and the surrounding regions are very dusty (Table 4) and the broadest component shows a moderately high velocity dispersion of 435 - 547  $\text{km s}^{-1}$  (Table 3). Based on spatially varying line profiles (Figure 3), dust reddening, temperature and density (Figure 8, Figure B.2), and velocity, we

postulate that this object is surrounded by multi-phase circumstellar medium ejected through stellar winds or previous eruptions.

5. The BPT diagram (Figure 12) shows that the main excitation source of Godzilla has a stellar origin. We rule out a Very Massive Star or Wolf-Rayet star since we do not detect stellar  $\text{He II}$  or  $\text{C IV}$  emission (Section 5.4).
6. We find that an LBV with a hotter companion (analogous to  $\eta$  Car) best qualitatively explains our observations simultaneously without requiring unrealistically high magnification. Gas condensations exposed to more intense radiation emitted by an LBV star compared to the Weigelt blobs, can be an alternative scenario. Considering (1) that the measured maximum velocity of the broadest component of  $\text{H}\alpha$  in Godzilla is an order of magnitude smaller than that of  $\eta$  Car during the Great Eruption (Figure 6, Section 4.2) and (2) the non-detection of P Cygni profiles, we suggest that the main component of Godzilla might be an LBV at the post-giant eruption phase which is still maintaining relatively high luminosity. We point out that a spectroscopic monitoring program of Godzilla could determine whether there is periodic variations in nebular emission lines, such as the 5.54-year spectroscopic period seen for  $\eta$  Car.

“Godzilla” is a truly remarkable object. The evidence strongly disfavors previous suggestions that it is a supernova, leading to the conclusion that it must be an object with luminosity comparable to a single stellar object, extremely magnified by alignment with microcaustics along the optical path. In addition to existing clues in the literature, we find strong spectroscopic evidence pointing to the object being an  $\eta$  Car analog with very dense, neutral gas condensations, possibly with a smaller, hot, blue companion. The presence of strong forbidden and  $\text{H I}$  recombination emission suggests that this object is likely embedded in a larger, but much less magnified,  $\text{H II}$  region. Future investigation of possible spectral variability and refined lens models may help further constrain the nature of Godzilla.

*Acknowledgements.* The authors would like to thank Seán Brennan, Raghild Lunnan and Yang Hu, Stockholm University, for helpful discussions about late stage evolution of massive stars. This work is in part based on observations made with the NASA/ESA/CSA James Webb Space Telescope. The data were obtained from the Mikulski Archive for Space Telescopes at the Space Telescope Science Institute, which is operated by the Association of Universities for Research in Astronomy, Inc., under NASA contract NAS 5-03127 for JWST. These observations are associated with program #2555. Support for program #2555 was provided by NASA through a grant from the Space Telescope Science Institute, which is operated by the Association of Universities for Research in Astronomy, Inc., under NASA contract NAS 5-03127. ER-T is supported by the Swedish Research Council grant Nr. 2022-04805\_VR. This work makes use of the software packages Astropy (The Astropy Collaboration et al. 2013, 2018, 2022), Matplotlib (Hunter 2007), NumPy (Harris et al. 2020), Uncertainties Python package by Eric O. LEBIGOT, Jupyter notebook (Kluyver et al. 2016), LMFIT (Newville et al. 2014) and PyNeb (Luridiana et al. 2015).

## References

- Abraham, Z., Beaklini, P. P. B., Cox, P., Falceta-Gonçalves, D., & Nyman, L.-Å. 2020, *Monthly Notices of the Royal Astronomical Society*, 499, 2493
- Abraham, Z., Falceta-Gonçalves, D., & Beaklini, P. P. B. 2014, *The Astrophysical Journal*, 791, 95
- Bowen, I. S. 1934, *Publications of the Astronomical Society of the Pacific*, 46, 146
- Calzetti, D., Armus, L., Bohlin, R. C., et al. 2000, *The Astrophysical Journal*, 533, 682
- Chen, W., Kelly, P. L., Diego, J. M., et al. 2019, *The Astrophysical Journal*, 881, 8
- Conti, P. S. 1984, 105, 233
- Cullen, F., Shapley, A. E., McLure, R. J., et al. 2021, *Monthly Notices of the Royal Astronomical Society*, 505, 903

- Dahle, H., Aghanim, N., Guennou, L., et al. 2016, *Astronomy and Astrophysics*, 590, 2
- Damineli, A. 1996, *The Astrophysical Journal*, 460, L49
- Davidson, K. & Humphreys, R. M., eds. 2012, *Astrophysics and Space Science Library*, Vol. 384, *Eta Carinae and the Supernova Impostors* (Boston, MA: Springer US)
- de Groot, M. 1988, *Irish Astronomical Journal*, 18, 163
- Diego, J. M. 2019, *Astronomy and Astrophysics*, 625, A84
- Diego, J. M., Kaiser, N., Broadhurst, T., et al. 2018, *The Astrophysical Journal*, 857, 25
- Diego, J. M., Meena, A. K., Adams, N. J., et al. 2023a, *Astronomy and Astrophysics*, 672, A3
- Diego, J. M., Pascale, M., Kavanagh, B. J., et al. 2022, *Astronomy and Astrophysics*, 665 [arXiv: 2203.08158]
- Diego, J. M., Sun, B., Yan, H., et al. 2023b, *Astronomy and Astrophysics*, 679, A31
- Draine, B. T. 2011, *Physics of the Interstellar and Intergalactic Medium*
- Fernández-Lajús, E., Fariña, C., Torres, A. F., et al. 2009, *Astronomy and Astrophysics*, 493, 1093
- Fudamoto, Y., Sun, F., Diego, J. M., et al. 2024, *JWST Discovery of \$40+\$ $\mu$ m Microlensed Stars in a Magnified Galaxy, the "Dragon" behind Abell 370*
- Furtak, L. J., Meena, A. K., Zackrisson, E., et al. 2024, *Monthly Notices of the Royal Astronomical Society*, 527, L7
- Grandi, S. A. 1980, *The Astrophysical Journal*, 238, 10
- Guseva, N. G., Thuan, T. X., & Izotov, Y. I. 2023, *Monthly Notices of the Royal Astronomical Society*, stad3485
- Haisch, B. M., Linsky, J. L., Weinstein, A., & Shine, R. A. 1977, *The Astrophysical Journal*, 214, 785
- Harris, C. R., Millman, K. J., Van Der Walt, S. J., et al. 2020, *Nature*, 585, 357
- Herrero, A., Garcia, M., Uytterhoeven, K., et al. 2010, *Astronomy and Astrophysics*, 513, A70
- Humphreys, R. M., Davidson, K., & Smith, N. 1999, *Publications of the Astronomical Society of the Pacific*, 111, 1124
- Hunter, J. D. 2007, *Computing in Science & Engineering*, 9, 90
- Immmer, S., Fesen, R. A., Van Dyk, S. D., et al. 2005, *The Astrophysical Journal*, 632, 283
- Johansson, S. & Letokhov, V. S. 2005, *Monthly Notices of the Royal Astronomical Society*, 364, 731
- Kauffmann, G., Heckman, T. M., Tremonti, C., et al. 2003, *Monthly Notices of the Royal Astronomical Society*, 346, 1055
- Kaurov, A. A., Dai, L., Venumadhav, T., Miralda-Escudé, J., & Frye, B. 2019, *The Astrophysical Journal*, 880, 58
- Kelly, P. L., Chen, W., Alfred, A., et al. 2022, *Flashlights: More than A Dozen High-Significance Microlensing Events of Extremely Magnified Stars in Galaxies at Redshifts  $Z=0.7-1.5$*
- Kelly, P. L., Diego, J. M., Rodney, S., et al. 2018, *Extreme Magnification of a Star at Redshift 1.5 by a Galaxy-Cluster Lens*
- Kewley, L. J., Dopita, M. A., Sutherland, R. S., Heisler, C. A., & Trevena, J. 2001, *The Astrophysical Journal*, 556, 121
- Kewley, L. J., Nicholls, D. C., & Sutherland, R. S. 2019, *Annual Review of Astronomy and Astrophysics*, 57, 511
- Khatami, D. & Kasen, D. 2023, *The Landscape of Thermal Transients from Supernova Interacting with a Circumstellar Medium*
- Kluyver, T., Ragan-Kelley, B., Pérez, F., et al. 2016, *Jupyter Notebooks—a Publishing Format for Reproducible Computational Workflows*, 87–90
- Kramida, A. & Ralchenko, Y. 1999, *NIST Atomic Spectra Database, NIST Standard Reference Database 78*
- Luridiana, V., Morisset, C., & Shaw, R. A. 2015, *Astronomy & Astrophysics*, 573, A42
- Mainali, R., Rigby, J. R., Chisholm, J., et al. 2022, *The Astrophysical Journal*, 940, 160
- Makarov, D. I., Makarova, L. N., Pustilnik, S. A., & Borisov, S. B. 2017, *Monthly Notices of the Royal Astronomical Society*, 466, 556
- Mauerhan, J. C., Smith, N., Silverman, J. M., et al. 2013, *Monthly Notices of the Royal Astronomical Society*, 431, 2599
- Meena, A. K., Zitrin, A., Jiménez-Teja, Y., et al. 2023, *The Astrophysical Journal*, 944, L6
- Mehner, A., Davidson, K., Ferland, G. J., & Humphreys, R. M. 2010, *The Astrophysical Journal*, 710, 729
- Milisavljevic, D., Fesen, R. A., Chevalier, R. A., et al. 2012, *The Astrophysical Journal*, 751, 25
- Miralda-Escude, J. 1991, *The Astrophysical Journal*, 379, 94
- Newville, M., Stensitzki, T., Allen, D. B., & Ingargiola, A. 2014, *LMFIT: Non-Linear Least-Square Minimization and Curve-Fitting for Python*, [object Object]
- Pascale, M. & Dai, L. 2024, *A Young Super Star Cluster Powering a Nebula of Retained Massive Star Ejecta*
- Rigby, J. R., Bayliss, M. B., Sharon, K., et al. 2018, *The Astronomical Journal*, 155, 104
- Rivera-Thorsen, T. E., Dahle, H., Chisholm, J., et al. 2019, *Science*, 366, 738
- Rivera-Thorsen, T. E., Dahle, H., Gronke, M., et al. 2017, *Astronomy and Astrophysics*, 608, 1
- Rodney, S. A., Balestra, I., Bradac, M., et al. 2018, *Nature Astronomy*, 2, 324
- Sharon, K., Mahler, G., Rivera-Thorsen, T. E., et al. 2022, *The Astrophysical Journal*, 941, 203
- Shore, S. N. & Wahlgren, G. M. 2010, *Astronomy and Astrophysics*, 515, A108
- Smith, N. 2019, *Monthly Notices of the Royal Astronomical Society*, 489, 4378
- Smith, N., Rest, A., Andrews, J. E., et al. 2018, *Monthly Notices of the Royal Astronomical Society*, 480, 1457
- Smith, N. & Tombleson, R. 2015, *Monthly Notices of the Royal Astronomical Society*, 447, 598
- Steidel, C. C., Strom, A. L., Pettini, M., et al. 2016, *The Astrophysical Journal*, 826, 159
- Strom, A. L., Rudie, G. C., Trainor, R. F., et al. 2023, *CECILIA: The Faint Emission Line Spectrum of Z~2-3 Star-forming Galaxies*
- Tachiev, G. & Fischer, C. F. 2001, *Canadian Journal of Physics*, 79, 955
- The Astropy Collaboration, Price-Whelan, A. M., Lim, P. L., et al. 2022, *The Astrophysical Journal*, 935, 167
- The Astropy Collaboration, Price-Whelan, A. M., Sipőcz, B. M., et al. 2018, *The Astronomical Journal*, 156, 123
- The Astropy Collaboration, Robitaille, T. P., Tollerud, E. J., et al. 2013, *Astronomy & Astrophysics*, 558, A33
- Topping, M. W., Shapley, A. E., Reddy, N. A., et al. 2020a, *Monthly Notices of the Royal Astronomical Society*, 499, 1652
- Topping, M. W., Shapley, A. E., Reddy, N. A., et al. 2020b, *Monthly Notices of the Royal Astronomical Society*, 495, 4430
- Vanzella, E., Meneghetti, M., Pastorello, A., et al. 2020, *Monthly Notices of the Royal Astronomical Society: Letters*, 499, L67
- Venumadhav, T., Dai, L., & Miralda-Escudé, J. 2017, *The Astrophysical Journal*, 850, 49
- Weigelt, G. & Ebersberger, J. 1986, *Astronomy and Astrophysics*, 163, L5
- Weis, K. & Bomans, D. J. 2020, *Luminous Blue Variables*
- Weisenbach, L., Anguita, T., Miralda-Escudé, J., et al. 2024, *Microlensing near Macro-Caustics*
- Welch, B., Coe, D., Diego, J. M., et al. 2022a, *Nature*, 603, 815
- Welch, B., Coe, D., Zackrisson, E., et al. 2022b, *The Astrophysical Journal Letters*, 940, L1
- Wofford, A., Ramírez, V., Lee, J. C., et al. 2020, *Monthly Notices of the Royal Astronomical Society*, 493, 2410
- Wolf, B. 1989, *Astronomy and Astrophysics*, 217, 87

## Appendix A: Spectra

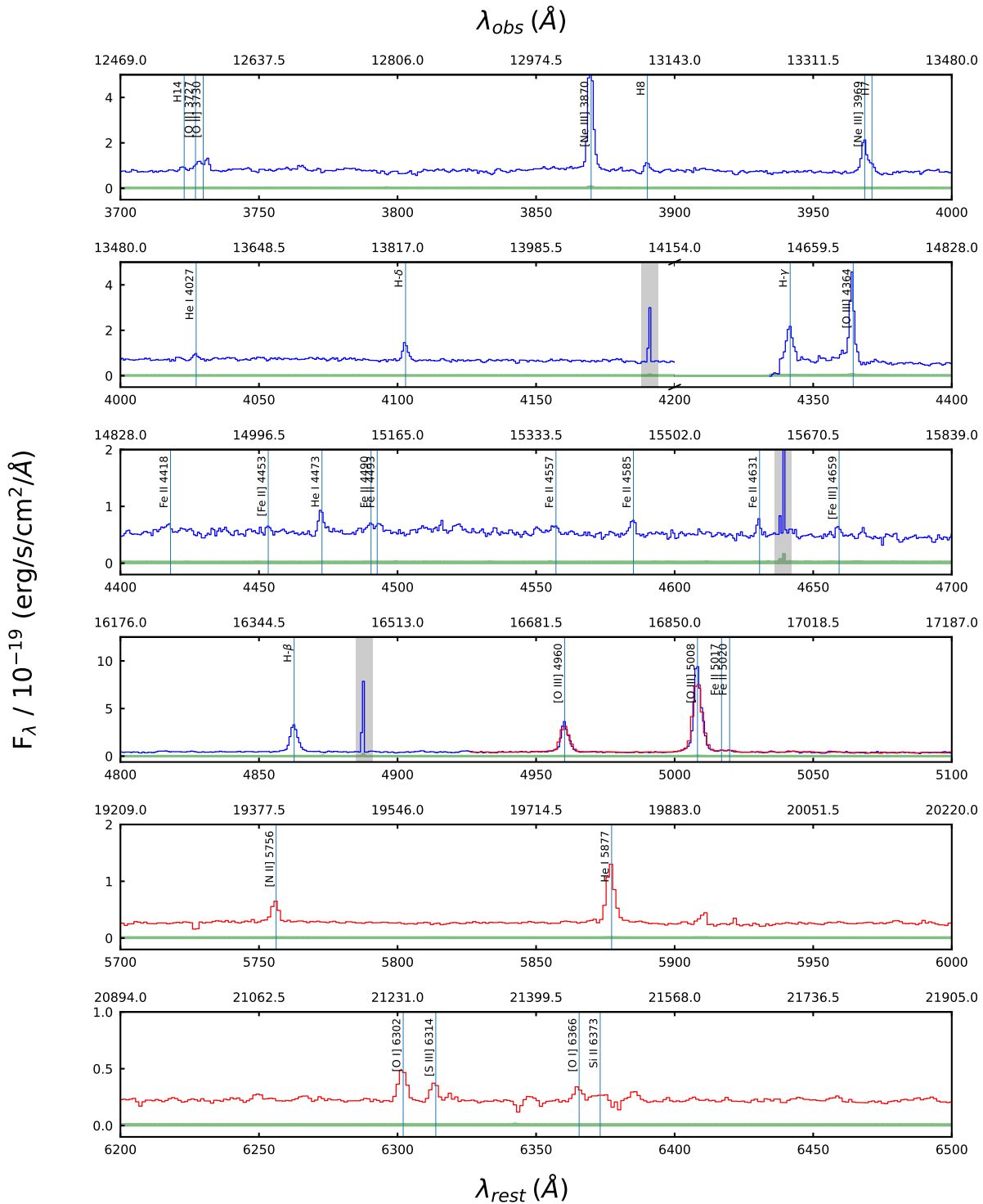


**Fig. A.1.** One-dimensional spectrum from the bright central region of Godzilla. Observed-frame flux densities from the G140H/F100LP and G235H/F170LP gratings are shown in blue and red solid lines, respectively. Standard deviation is shown with green area and hot/noisy pixels are marked with grey shades.



## Appendix B: Properties in surroundings

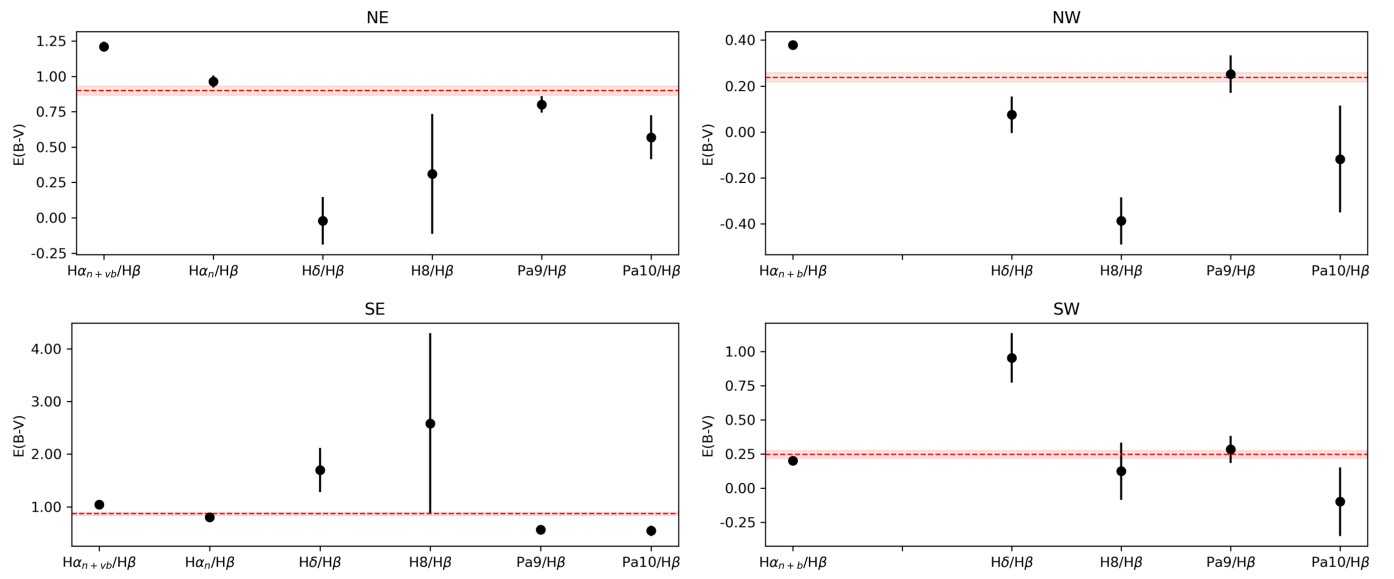


**Fig. B.1.**  $E(B - V)$  computed for the NE, SE, NW, SW regions in the same manner as [Figure 7](#).

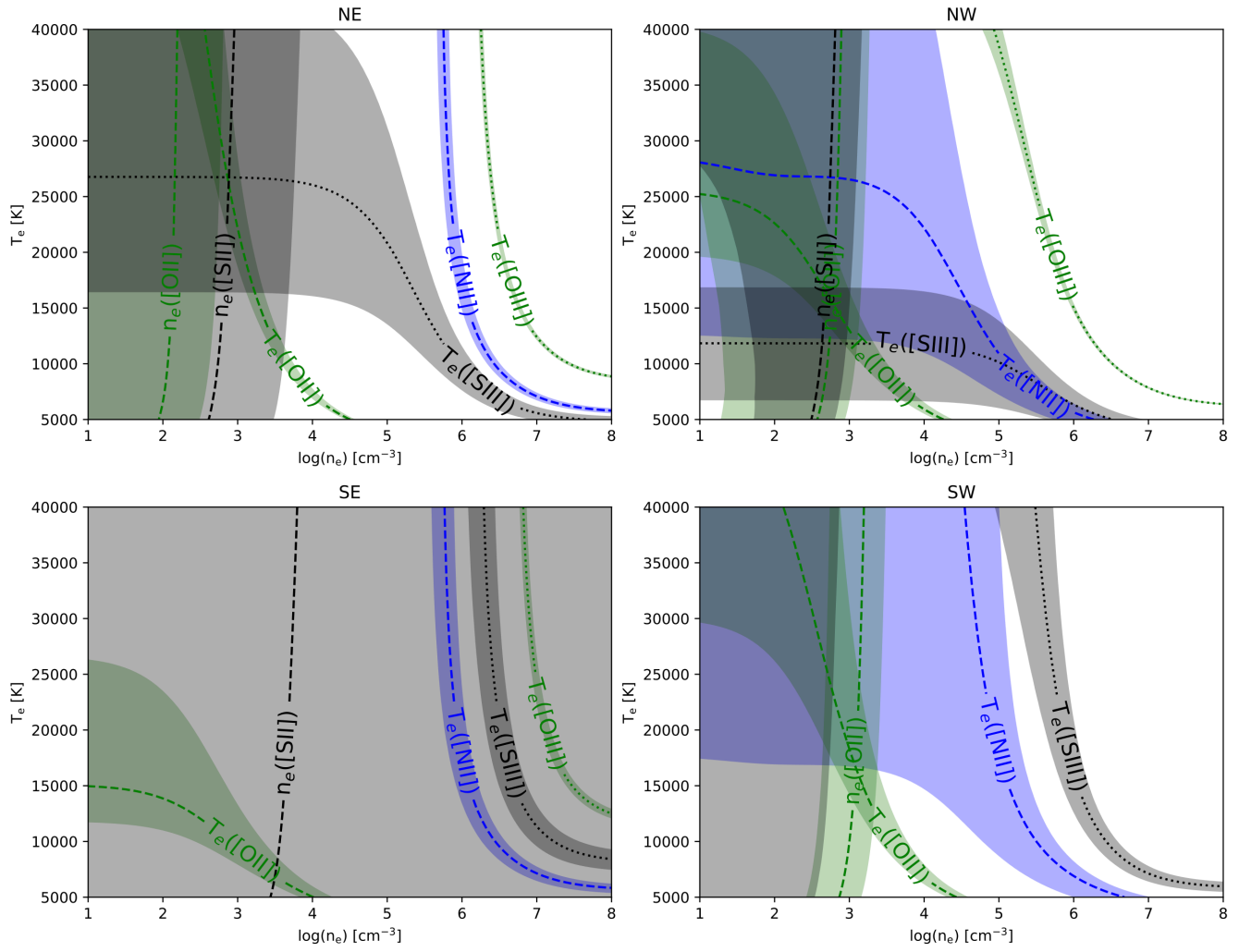


**Fig. B.2.** Joint temperature and density solutions computed with PyNeb for the NE, SE, NW, SW regions, using the same nebular lines as found in Figure 8.